sustainability

MDPI

Article

Adsorption–Desorption Behavior of the Antibiotic Ofloxacin in Calcium-Rich Sediments at Riverbank Sewage Discharge Outlets: Implications for Sustainable Water Quality Management in an Arid Inland River Basin

Xiao Wang [1], Rensheng Lv [2], Tianwei Qi [1], Xiaolan Ma [1], Pengguo Liu [1], Bingjie Wang [1], Abdulla Huxitar [1] and Yanyan Ge [3,*]

[1] Key Laboratory of Green and Efficient Mining and Ecological Restoration in High-Altitude Arid Regions of Xinjiang, Urumqi 830047, China; w3208513647@163.com (X.W.); 15751918082@163.com (T.Q.); mxl147258368@outlook.com (X.M.); li514983liu20@163.com (P.L.); 17881150533@163.com (B.W.); 18997660989@163.com (A.H.)

[2] College of Ecology and Environment, Xinjiang University, Urumqi 830017, China; jxgxlrs@sina.com

[3] School of Geology and Mining Engineering, Xinjiang University, Urumqi 830046, China

* Correspondence: geyanyan0511@xju.edu.cn

Abstract

Fluoroquinolone antibiotics are widely detected emerging pollutants, yet their interfacial behavior in the alkaline, calcium-rich sediments of arid inland river basins remains poorly quantified, which limits regional risk assessment. This study selected riverbank calcareous sediments from the Ili River and ofloxacin (OFL), a representative fluoroquinolone, and used batch adsorption–desorption experiments to quantify the retention of OFL and the regulatory roles of pH and coexisting cations. Adsorption was biphasic, with a fast stage (<1 min) followed by slow equilibration, and equilibrium was approached within 8 h. When the pseudo-first-order (PFO), pseudo-second-order (PSO), and Elovich models were all fitted by nonlinear least squares on the original q-t scale, the Elovich model gave the best description at both 1 and 10 mg L^{-1} (R^2 = 0.829 and 0.589, lowest AIC), whereas PFO and PSO performed poorly over the full time range (R^2 = 0.20–0.53). Boyd analysis indicates that particle diffusion dominates for the two XFD datasets, whereas a significant positive intercept in a second sediment series shows that film diffusion also contributes. Desorption kinetics were also best described by the Elovich model (R^2 = 0.929). Isotherm analysis with 4–11 data points per temperature (rather than the three points used previously) showed that the Langmuir and Freundlich models fit the data comparably, so the results do not justify discriminating between monolayer and multilayer uptake (difference in AIC $\leq$ 1 at 15 and 35 °C, and 6.5 in favor of Langmuir at 25 °C); the corresponding Dubinin–Radushkevich mean free energy of 0.08–0.25 kJ mol^{-1} indicates physisorption-dominated uptake. Thermodynamic parameters calculated from the 15/25/35 °C series by the van't Hoff relation gave Delta-G = −20 kJ mol^{-1} (spontaneous), Delta-H = −14.5 ± 13.2 kJ mol^{-1}, and Delta-S = 20.5 ± 44.3 J mol^{-1} K^{-1}, i.e., a weakly exothermic, entropy-assisted process whose enthalpy term is not statistically significant; the 5/15/25 °C series was non-monotonic and is therefore not used to derive the enthalpy. Desorption exceeded adsorption (maximum desorbed/adsorbed ratio 106–136%) and the Freundlich-based hysteresis index rose from −0.09 at 5 °C to 0.37 at 25 °C, so part of the sorbed OFL is retained against desorption. Coexisting cations inhibited OFL adsorption through competition for surface sites, following the order Mg^{2+} > Ca^{2+} > Na^{+} at matched molarity (0.01 mol L^{-1}), and the inhibition intensified with increasing cation concentration. Because Na^{+} was applied at the same molarity as Mg^{2+} as an ionic-strength control while Ca^{2+} was also applied at

Check for updates

Academic Editors: Yanmei Li, Jesús Horacio Hernández Anguiano, Jorge Adrian Perera-Burgos and Alfredo González-Calderón

Received: 27 August 2026
Revised: 29 September 2026
Accepted: 9 October 2026
Published: 13 October 2026

Copyright: © 2026 by the authors. Licensee MDPI, Basel, Switzerland. This article is an open access article distributed under the terms and conditions of the Creative Commons Attribution (CC BY) license.

a higher concentration, the ranking reflects specific competition by the divalent cations combined with a weaker double-layer (ionic-strength) effect for the monovalent ion. Acidic pH enhanced adsorption and alkaline pH suppressed it, consistent with the change in OFL speciation from cationic through zwitterionic to anionic. This work quantifies the adsorption–desorption behavior of OFL on arid-region calcareous sediments and provides parameter values with uncertainty estimates that support risk assessment and pollution control in the Ili River Basin. From a sustainability perspective, the work converts these site-specific measurements into transferable, uncertainty-bounded parameters (Langmuir and Freundlich capacities, the linear partition coefficient Kd and the hysteresis index) for a sediment type that is widespread in arid inland river basins. It therefore supplies directly usable input for the definition and quantification of water-quality sustainability indicators, the monitoring of the sediment buffering function over time, and the setting of discharge-outlet effluent limits and the seasonal screening of secondary-pollution risk during the warm, low-flow irrigation period, thereby connecting a mechanistic sorption study to the wider objective of sustaining safe water use in a water-scarce region.

Keywords: ofloxacin; adsorption; desorption; coexisting ions; pH; capacity; emerging contaminants; risk assessment

1. Introduction

With the continuous expansion of global antibiotic production and usage, the issue of antibiotic residues in water environments, soil, and sediments has become increasingly severe, emerging as one of the key bottlenecks hindering sustainable development [1]. Antibiotics are typically discharged into water bodies either in their original form or through the emission of household wastewater or the discharge of expired medications as metabolites [2]. The frequency of detecting antibiotics in aquatic systems is steadily increasing [3]. Fluoroquinolones are widely present in pharmaceutical wastewater, municipal sewage, and groundwater, with concentrations ranging from μg/L to mg/L [4]. Norfloxacin (NOR) and ciprofloxacin (CIP) are quinolone-class antibacterial agents and among the most commonly used antibiotics [5], with broad applications in both human and veterinary medicine. In industrial wastewater and shrimp farming ponds, NOR concentrations have been detected at 6–31 mg/L, while CIP levels can reach 30 mg/L in wastewater from pharmaceutical plants [6]. Sulfamethoxazole (SMZ), a sulfonamide antibiotic widely used for treating urinary tract infections and respiratory infections [7], exhibits high detection frequencies and elevated concentrations; for instance, SMZ levels in wastewater from sewage treatment plants can reach 0.22–2.20 μg/L [8], whereas in household and medical wastewater, concentrations may attain mg/L levels per liter [9]. It is estimated that China produces approximately 248,000 tons of antibiotics annually, with 90% used for human purposes (48%) and animal treatment (42%), and the remaining 10% exported [10]. The extensive use of antibiotics inevitably leads to their discharge into aquatic systems [11]. Since 2022, antibiotics have been consistently listed in China's Government Work Report as part of efforts to address new pollutants, classified as a major environmental issue in China, and subject to a series of policies aimed at strengthening their management [12,13]. Conducting in-depth research on the adsorption, desorption, migration, and transformation behaviors of antibiotics in environmental media holds significant theoretical and practical value for the scientific assessment of their ecological risks and the formulation of precise prevention and control strategies [14].

Researchers worldwide have conducted extensive studies on the adsorption behavior of various antibiotics in different environmental media [15]. Batch equilibrium experiments

combined with kinetic and isothermal adsorption models are commonly employed to elucidate their adsorption patterns and mechanisms [16].

Studies by Wang L et al. on sediments from typical tributaries of the Yellow River [17], as well as research by Huang Qingli et al. on OFL adsorption onto carbon-based adsorbents [18], have both confirmed that the quasi-second-order kinetic model provides a higher goodness-of-fit for the adsorption process, indicating that chemical interactions constitute the core control mechanism for the adsorption rate. Qin Xiaopeng's investigation into OFL adsorption in tropical soils [19] and Yi Lili's study on ciprOFL adsorption in loess [20] both revealed that the adsorption process generally exhibits a two-stage characteristic of "rapid adsorption followed by slow equilibration". During the initial stage, the antibiotic rapidly occupies the active sites on the medium surface. As these sites gradually become saturated, the adsorption rate continues to decelerate, with the equilibrium time typically ranging from several hours to dozens of hours. Fu L et al.'s [21] research on microplastic systems demonstrated that adsorption is not governed solely by intraparticle diffusion but rather involves a synergistic interaction between liquid film diffusion and intraparticle diffusion, where liquid film diffusion predominates initially, while the limiting effect of intraparticle diffusion becomes increasingly prominent during the middle and later stages [22]. For heterogeneous media with complex components such as sediments, the Elovich model can effectively reflect the dynamic changes in the adsorption activation energy, further corroborating that adsorption is a comprehensive process involving both surface reactions and diffusion.

Studies on complex media such as natural soils and sediments generally find that both models fit the data well over the limited concentration ranges that are usually investigated [23]; however, a good simultaneous fit does not demonstrate that monolayer and multilayer uptake operate together because, over a restricted concentration range, the two models often describe the same data equally well. Discriminating between them requires a model that explicitly represents multilayer coverage, such as the BET model, and a claim of chemisorption requires independent evidence such as spectroscopic analysis or the Dubinin–Radushkevich mean free energy [24].

Existing studies have confirmed that environmental factors, such as pH value, coexisting ions, dissolved organic matter, and temperature, are key determinants of antibiotic adsorption behavior [25]. These factors profoundly regulate the driving force and capacity of the adsorption process by altering the molecular structure, surface charge properties, and active sites on the adsorbent surface [26]. However, most existing research has focused on neutral or acidic soil environments, while studies investigating antibiotic adsorption behavior in soils under the specific alkaline and high-calcium conditions characteristic of arid regions remain relatively scarce. Under the unique pedogenic conditions of arid regions, soils generally exhibit elevated pH values and are rich in calcium carbonate as well as free calcium and magnesium ions. This distinctive geochemical background leads to significant variations in the distribution behavior of antibiotics at the solid–liquid interface [27]. For example, under high-pH conditions, antibiotics may predominantly exist in anionic or zwitterionic forms [28], which contrasts sharply with their predominantly cationic form observed under acidic conditions, thereby reversing electrostatic repulsion or attraction effects. Simultaneously, high concentrations of Ca^{2+} and Mg^{2+} not only inhibit antibiotic adsorption through competitive adsorption but may also act as ion bridges to facilitate the complexation adsorption of antibiotic anions with negatively charged soil colloids [29].

The funnel-shaped Ili River Valley, which opens to the west, has been proposed to guide wind-driven air currents that transport silt particles and deposit them on river valley terraces and foothill hills. This mixed genesis, dominated by aeolian processes with a local superposition of flood deposits during the cold, arid phases of the Last Glacial Period, is

an inference drawn from regional Quaternary studies rather than a result of the present dataset, and it is stated here as such. The sediments sampled for this work were taken from the alluvial plain of the Ili River (Section 3.1.2), and are described below on the basis of their measured mineralogy. The sediment consists predominantly of silt-sized detritus composed of clastic minerals, carbonates, and clay minerals. Calcite is almost entirely resistant to leaching or loss, remaining extensively within the pore spaces and at the particle–soil interface, resulting in a high calcium content. However, the characteristics and mechanisms of antibiotic adsorption and desorption in this medium, and the factors that control them, remain unclear. These complex interactions are not yet fully elucidated and require further experimental and analytical study. This knowledge gap hinders our understanding of the migration and transformation of antibiotics in soil-water systems of arid regions and limits the accurate assessment of antibiotic ecological risk and environmental capacity in such areas, so targeted and in-depth research is needed to fill this scientific void.

This study focuses on calcareous sediments near sewage discharge outlets along the Ili River, selecting the typical fluoroquinolone antibiotic OFL as the target pollutant. Through systematic batch equilibrium experiments, this study elucidates the adsorption kinetics and thermodynamic behavior of OFL in alkaline calcareous soils under arid conditions, revealing how key environmental factors like pH levels and coexisting cations regulate its adsorption and desorption behavior. The physical and chemical properties of the soil are used to explore microscopic adsorption mechanisms under specific environmental contexts to fill the knowledge gap in the existing research. To achieve these objectives, this study encompasses the following specific components: investigation of the adsorption–desorption kinetic characteristics of OFL on calcareous sediments, examination of the isothermal adsorption–desorption behavior and thermodynamic patterns of OFL on calcareous sediments, analysis of the regulatory effects of key environmental factors on adsorption–desorption behavior, and elucidation of the adsorption–desorption mechanism of OFL on calcareous sediments.

This study systematically analyzes the adsorption/desorption kinetics of OFL, its isothermal adsorption characteristics, and the effects of pH and coexisting ion composition. It also conducts an in-depth exploration of its adsorption and desorption mechanisms. The objective of this research is to accurately evaluate the dual role of alkaline calcareous sediments at sewage discharge outlets in the Ili River Basin as both a “sink” and a “source” for antibiotics, thereby providing a theoretical basis for regional pollution control efforts.

From the standpoint of sustainability, the significance of this work lies in converting an environmental-process study into an operational input for water-resource management. By quantifying how the calcareous sediments that line the sewage discharge outlets of the Ili River retain and subsequently release ofloxacin, the present study moves the assessment of pollution risk from a qualitative description towards measurable and monitorable indicators: the partition coefficient, desorption ratio, and hysteresis index obtained here can serve as quantitative metrics of the buffering function of riverbank sediments and be tracked through time to detect the loss of that function. This study thereby addresses two central concerns of sustainability research, namely, the definition and quantification of sustainability and the measurement and monitoring of it.

The results also have a practical dimension for sustainability tools and applications. The kinetic and isotherm parameters reported here, together with their uncertainty ranges, are the input required by the reactive-transport and risk-screening models with which regional authorities derive effluent limits and schedule sediment monitoring. Identifying pH, temperature, and ionic strength as the controlling variables shows which environmental levers are worth acting on, and the reversibility of adsorption quantified here provides a scientific basis for the requirements of discharge-outlet management and the control

of emerging pollutants that appear in relevant water-pollution prevention and control regulations. In this way, this paper connects laboratory-scale sorption behavior to the instruments of environmental governance in water-scarce basins.

2. Overview of the Study Area

The Ili River, as the river system with the most abundant water resources within the Xinjiang Uygur Autonomous Region, not only plays a vital role in supplying regional water resources but also serves as a transboundary river with significant international influence [30]. Its ecological health directly impacts the stability of the ecological security barrier along China's western frontier and holds a crucial strategic position in the allocation of water rights for international rivers and the governance of cross-border water environments [31]. The river basin encompasses traditional high-quality livestock breeding bases in China, where the livestock farming industry is extensive, and antibiotics are widely used for disease prevention and control as well as to enhance feed efficiency [32]. Previous studies have indicated that, influenced by the hydrological cycle characteristics under arid and semi-arid climatic conditions, antibiotic pollutants continuously migrate and accumulate in the soil environment along the Ili River through various pathways, such as the application of livestock manure composted for field use, discharge of livestock wastewater, and direct discharge from pollution outlets, resulting in a concerning pollution load and diffusion pattern [33].

The Ili River Basin is located at the westernmost end of the Tianshan Mountains in Xinjiang, surrounded by mountains on three sides, with a trumpet-shaped topography opening toward the west (Figure 1). It exhibits a typical temperate continental climate, characterized by an average annual temperature of 11.2 °C, annual precipitation of 413.6 mm, mild and humid conditions, significant diurnal temperature variations, ample sunshine, and abundant rainfall, thereby forming a "wet island" within the arid region [34]. As the primary surface water body in the region, the Ili River basin covers an area of approximately 58,000 square kilometers, with an average annual runoff reaching 16.7 billion cubic meters. Its main tributaries include the Tekes River, Gongnaisi River, Kashgar River, and Horgos River. These tributaries converge into the Ili River before flowing into Lake Balkhash in Kazakhstan [35]. The Ili River watershed is well-developed, with its runoff primarily sourced from mountainous precipitation and glacial meltwater, exhibiting distinct wet and dry seasons. These hydrological characteristics directly influence the fluctuations in groundwater levels within the riverbank zones and the processes of pollutant migration and transformation. Research sampling points were established near the river discharge outlets, where the soil types predominantly consist of tidal soils or alluvial soils, soils that have long been subjected to sewage irrigation and surface runoff, posing potential accumulation risks for emerging pollutants such as antibiotics, making this area an ideal site for studying the adsorption behavior of antibiotics in the soil environment [36].

Of particular concern is that the primary soil types in the Ili River Valley are black calcareous soils and chestnut calcareous soils. These soils typically exhibit a neutral to strongly alkaline pH, with pH values generally ranging between 7.5 and 8.5 [37]. The soil matrix contains relatively high amounts of carbonate minerals and is rich in calcium components. Constrained by semi-arid climatic conditions, the decomposition rate of organic matter is rapid, resulting in generally low overall accumulation levels of organic matter. Within this typical environmental context characterized by high alkalinity and high calcium ion concentration, the migration and transformation behavior of antibiotics—particularly for compounds such as tetracyclines, which possess multi-step dissociation constants and readily form complexes with metal ions—will undergo significant changes in their speciation, solubility, and reactivity, thereby profoundly influencing interface

processes such as adsorption–desorption and migration and transformation between soil particles and pore water [38].

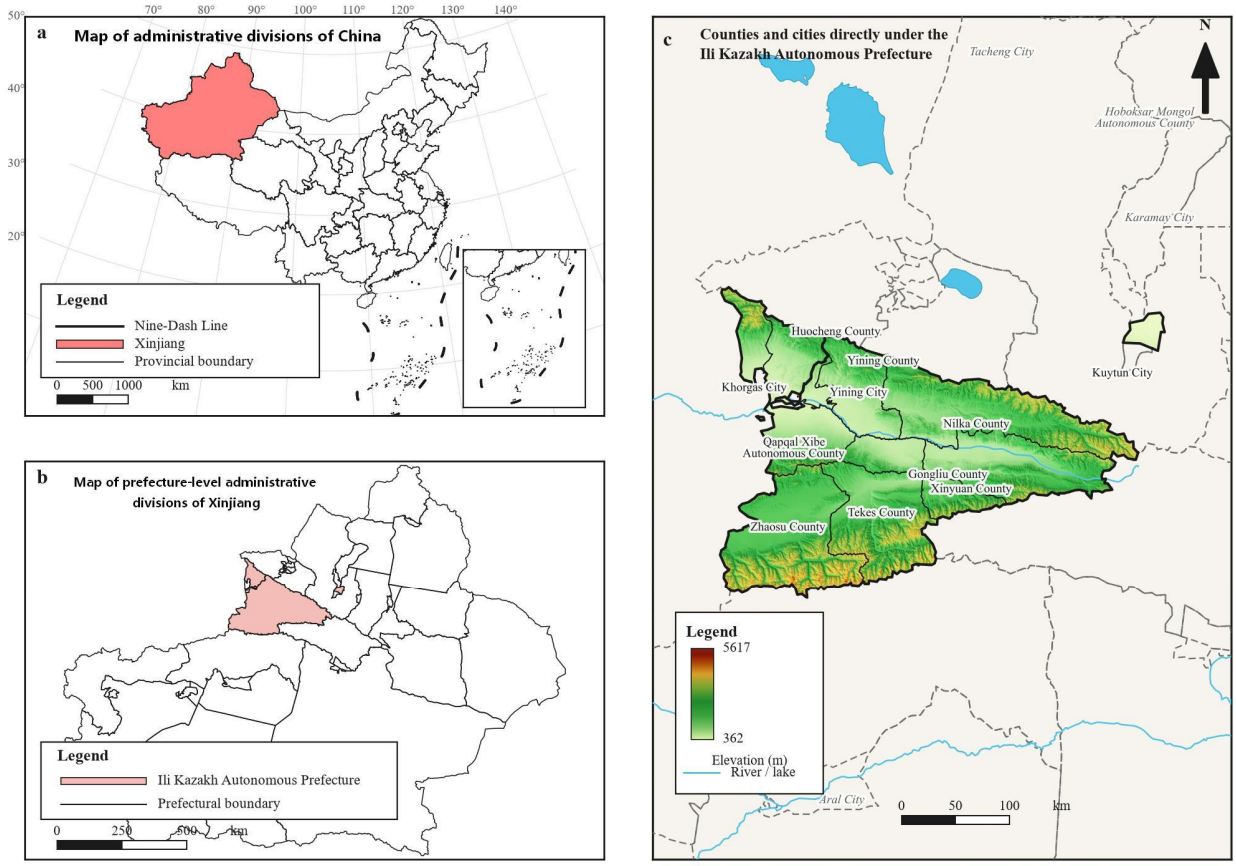


Figure 1. Overview of the study area.

River discharge outlets serve as critical pathways through which terrestrial pollutants enter the main stream of water bodies. The surrounding soil, having been subjected to long-term exposure to composite pollutant discharges rich in organic matter, nitrogen, phosphorus nutrients, and various antibiotics, has developed into a distinct contaminated zone that differs markedly from the surrounding natural soil, exhibiting exceptionally complex physicochemical properties [39]. Given the limited removal capacity of conventional wastewater treatment processes for strongly polar, highly water-soluble, and low-concentration antibiotics, adsorption technology—due to its advantages such as low cost, high treatment efficiency, and absence of toxic secondary metabolites—is widely regarded as one of the methods with the greatest application potential for controlling trace-level antibiotic pollution in water bodies and soils [40]. Therefore, conducting a systematic study of the adsorption kinetics and isothermal adsorption behavior of representative antibiotics in the soil surrounding typical discharge outlets of the Ili River will not only help elucidate the migration and immobilization mechanisms of such pollutants in complex real-world environments but will also provide a crucial scientific basis for assessing regional ecological risks and formulating targeted remediation strategies.

3. Sample Collection, Testing, and Analysis Methods

3.1. Sediment Sample Collection

3.1.1. Sample Collection

To systematically investigate the impact of sewage discharge outlets on the adsorption characteristics of antibiotics in soil, sampling points were established using a systematic site

selection method combined with expert judgment-based site selection methods, ensuring sample representativeness and scientific rigor [41]. In the affected area surrounding the sewage discharge outlet, sampling points were set around the outlet along the Ili River at specific locations corresponding to the flow direction, with separate sampling points established at different positions to analyze the distribution patterns of antibiotics. Control points were established upstream of the sewage discharge outlet or in areas where environmental conditions are consistent with those in the affected zone to compare pollution levels. To facilitate the analysis of antibiotic migration characteristics, surface soil samples were collected from each sampling point [42]. Sampling points were located using handheld GPS devices, during which surface environmental information—including geographic coordinates, elevation, vegetation coverage, and distance from the sewage discharge outlet—was recorded.

Samples were collected during the late high-flow period of the Ili River, when the river water level had declined but the soil moisture content remained high. Under these conditions, the inputs from the sewage outlet and the groundwater recharge jointly influence the soil moisture, and antibiotic distribution is highly active, making this a favorable time for studying adsorption kinetics [43]. No significant precipitation occurred in the three days preceding sampling, and the soil moisture content remained stable, thereby avoiding interference from rainfall.

Specific sampling procedures: First, remove surface litter and debris. At each sampling point, collect 3–5 subsamples using the "S"-shaped or plum blossom-shaped sampling layout, mix these subsamples, and then perform a quartering process to reduce the sample volume, retaining approximately 1 kg of soil as a representative sample. Sampling shall be conducted using non-metallic tools such as wooden shovels, bamboo strips, or plastic shovels; for soft surface soils, stainless steel soil augers may be employed [44]. Strict quality control measures must be implemented to prevent cross-contamination: after collecting each sample, tools should be cleaned and gloves replaced. Additionally, transport blank samples should be prepared to monitor for potential contamination. On-site, a portable multi-parameter analyzer shall be used to measure soil temperature, with three measurements taken at each sampling point. Ring cutter samples of intact soil shall be collected to determine soil bulk density and porosity—these parameters provide essential support for interpreting adsorption test results. After collection, the soil samples shall be placed in sealed bags or glass vials, air-exhausted, sealed, stored away from light, and transported back to the laboratory in a portable refrigeration box maintained at approximately 4 °C.

Since antibiotics are semi-volatile organic pollutants and adsorption tests are required, freeze-drying was employed for sample pretreatment in order to prevent antibiotic redistribution and microbial degradation caused by the migration of liquid water. Fresh soil samples were first screened to remove plant residues and rock fragments and then vacuum freeze-dried for 48 h at −50 °C to a constant weight. After drying, the samples were crushed and passed through 2 mm and 0.25 mm sieves, with different sieve meshes being used in sequence to avoid cross-contamination [45]. The samples were then thoroughly mixed and divided into three aliquots: one for the adsorption tests, one for the physicochemical analyses, and one reserved for verification or supplementary determination. The aliquot intended for the adsorption tests was kept with its natural structure. Antibiotic analysis samples were stored at −20 °C in the dark and the physicochemical analysis samples at room temperature in the dark. All bottles were labeled and a sample ledger was maintained. Freeze-drying was chosen in preference to oven drying because heating at 105 °C would dissolve and reprecipitate part of the carbonate cement, collapse the interlayer space of the smectitic component, and alter the pore structure. Freeze-drying preserves the interlayer spacing and pore network, but it also removes the resident pore

water and therefore changes the amount of dissolved organic matter available to compete with OFL for surface sites. Because the same pretreatment was applied to every sample, the comparisons between the pH, temperature, and cation treatments remain internally consistent even if the absolute capacities are affected.

3.1.2. Sampling Points

The sampling sites are located on the alluvial plains along the Ili River, forming part of the intermountain basin of the Ili River Valley (Figure 2). The river's runoff is replenished by high-altitude snowmelt (spring thaw and summer glacier melt) and mountain precipitation, resulting in pronounced seasonal variations with particularly prominent spring and summer floods. The river exhibits moderate sediment loads and frequent alternations between deposition and erosion. The surrounding area is densely populated with farmland and large-scale agricultural zones, supported by an advanced irrigation system that has significantly altered the natural vegetation and soil structure.

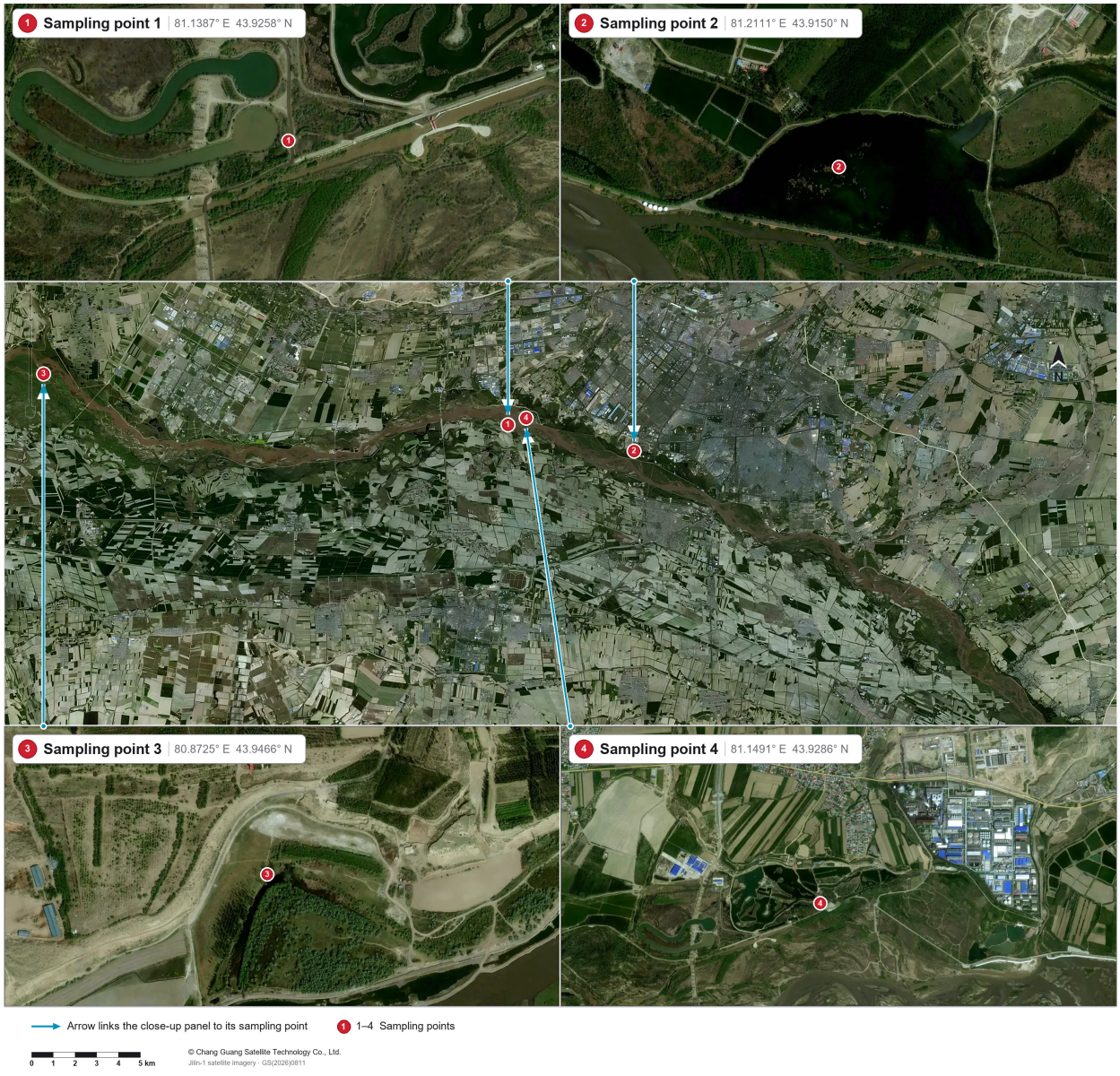


Figure 2. Sampling point map.

The sampled sediments are predominantly fluvial alluvium, formed by the weathering and deposition of detritus transported by the Ili River and its tributaries within the drainage basin. These sediments consist of calcareous deposits enriched in minerals such as potassium, calcium, and magnesium. In areas adjacent to agricultural land, fertilizer application has significantly increased the content of organic matter, nitrogen, and phosphorus in the surface sediments, although salt accumulation may also occur as a result of residual chemical fertilizer.

3.1.3. Test Samples

The sample consists of calcium-rich sediments whose fundamental physicochemical properties are dominated by three major components: a rigid framework (quartz ~31%, feldspar 40–46%); chemically active carbonate cementation phases (calcite 10–15%, dolomite 4%), which endow the sediment with significant potential for the release of Ca^{2+}, Mg^{2+}, and HCO_3^- and high sensitivity to acidic environments; and water-sensitive clay minerals (total ~7%, of which the illite/smectite mixed layer accounts for 20–28% with an interlayer smectite fraction of 65%), which are the primary contributors to the cation exchange capacity (CEC) and adsorption sites. The whole-rock and clay-fraction mineral contents were quantified by X-ray diffraction on two samples: XFH-002 and XFQ-002 (Tables 1 and 2); these are the same materials that were used in the batch experiments.

Table 1. Quantitative XRD analysis results of whole-rock minerals.

Sample Number	Quartz Qz	Potash Feldspar Kf	Plagioclase Pl	Calcite Cal	Dolomite Do	Amphibole Tm	Clay Minerals
XFH-002	30.67	16.72	28.99	10.35	4.03	2.50	6.73
XFQ-002	31.56	17.05	23.33	14.67	4.73	1.61	7.05

Table 2. Relative content of clay minerals (%), interlayer ratio.

Sample Number	Illite/Smectite Mixed Layer (I/S)	Illite It	Kaolinite Kao	Chlorite Chl	I/S Interlayer Ratio (s%)
XFH-002	27.92	43.54	6.03	22.51	65
XFQ-002	19.45	57.97	6.80	15.78	65

Textural characterization indicated a high bulk density and low porosity (total pore volume of only about 0.006 $cm^3\ g^{-1}$), with pores predominantly in the mesopore range (about 4 nm) and an estimated specific surface area (SSA) of 3–4 $m^2\ g^{-1}$. The SSA was estimated from the measured grain-size distribution and mineralogy; it was not determined by N2-BET physisorption, and this must be borne in mind when the value is compared with literature data. Similarly, the point of zero charge (pHPZC), total organic carbon content, and cation exchange capacity were not measured for these samples. These are acknowledged limitations of the present dataset: the SSA is the single most important parameter controlling the absolute adsorption capacity

Because the sediment was used as collected and not modified, its adsorption capacity is expected to be one to two orders of magnitude lower than that of the engineered adsorbents usually studied for ofloxacin removal. This difference in specific surface area, rather than any difference in surface chemistry, is the main reason why the capacities reported here are smaller than those in the engineered-adsorbent literature, and it is the appropriate basis for comparison.

Based on morphological characteristics, the sedimentary particles consist predominantly of irregular angular clasts with rough surfaces, bearing abundant flaky clay minerals

and exhibiting well-developed pores and fractures (Figure 3). Under high magnification, the clay minerals appear to exhibit a layered stacking structure, with nano-scale calcite grains distributed across their surfaces, thereby providing abundant surface sites for antibiotic adsorption.

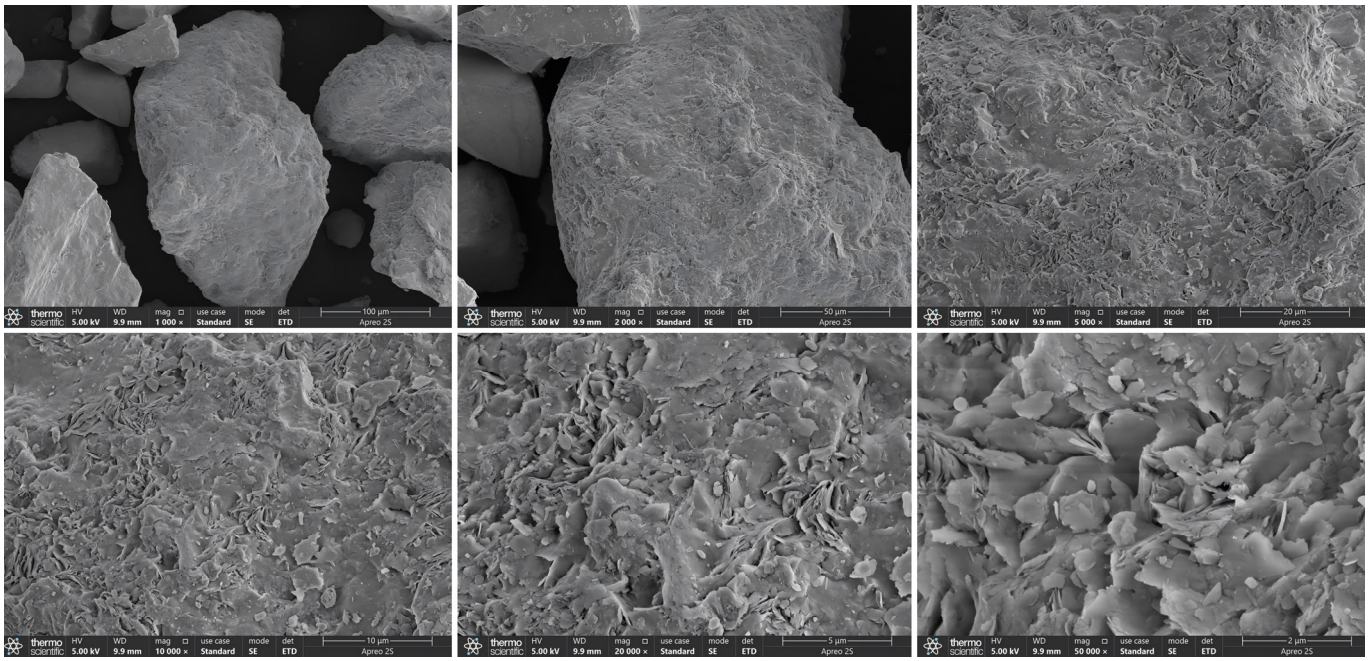


Figure 3. Scanning electron microscopy images of sediment samples at different magnifications.

The sediments collected from sampling points 1 and 2 were used for the primary adsorption–desorption batch test, while those from sampling points 3 and 4 were utilized for the comparative validation test. SEM and XRD analyses were performed on samples obtained from the lyophilized and sieved residues at sampling points 1 and 3, ensuring that the characterization subjects correspond precisely to the experimental subjects. The spatial distribution of sampling points reflects the gradient variation in the physicochemical properties of the sediments across different distances from the pollutant discharge outlet, whereas the characterization of the experimental samples elucidates, at the microscale level, the mineralogical and surface chemical basis underlying the adsorption capacity of the sediments for OFL.

3.2. Trial Protocol and Design

OFL is a third-generation fluoroquinolone synthetic broad-spectrum antibiotic. It is a typical bifunctional fluoroquinolone antibiotic that readily forms various interactions with adsorbents. It exhibits low solubility in water but high solubility in methanol, ethanol, acidic solutions, and alkaline solutions, along with strong chemical and thermal stability, making it resistant to decomposition in natural environments. Therefore, this study employed OFL as a representative antibiotic compound and utilized adsorption/desorption kinetic and adsorption/desorption thermodynamic experiments to compare the changes before and after the adsorption and desorption of the antibiotic (OFL), thereby providing a scientific assessment and prediction of the antibiotic profile in sediments collected from a wastewater discharge point in the Ili River [46]. The experimental protocol is as follows.

3.2.1. Main Experimental Instruments and Reagents

The primary instruments used in this experiment include: a gas-bath constant-temperature shaker produced by Tianjin Ouno Instrument Co., Ltd, China, Tianjin (model

HNY-200B); an acidity meter from Shanghai Youke Instrument & Meter Co., Ltd, China, Shanghai (model P901); and an electronic balance from Tianjin Tianma Hengji Instrument Co., Ltd, China, Tianjin (model FA124B). All reagents used in the experiment were of analytical grade (AR). Specifically, OFL was supplied by Shanghai Micron Biochemical Technology Co., Ltd, China, Shanghai;calcium ions (Ca^{2+}), sodium ions (Na^{+}), magnesium ions (Mg^{2+}), and bicarbonate ions (HCO_3^{-}) were all provided by Dongguan Jiajian Biotechnology Co., Ltd, China, Dongguan. Additionally, hydrochloric acid and sodium hydroxide were employed as common reagents in the experiment to perform key operations such as adjusting the pH value of solutions. These instruments and reagents collectively ensured the precise execution of the adsorption–desorption experiment, thereby guaranteeing the reliability and reproducibility of the data.

3.2.2. Adsorption/Desorption Kinetics Experiment Design

Prior to the commencement of the experiment, an OFL standard solution was prepared: a 1 L volumetric flask was selected as the reaction vessel to prepare OFL solutions with initial concentrations of 1 mg/L and 10 mg/L. The pH of the solutions was adjusted using a 0.1 mol/L sodium hydroxide solution to ensure that the OFL was in its optimal adsorption form, which was adjusted according to the capacity of the adsorbent. A number of test soil samples weighing 1.2 g (±0.01 g) were weighed (the soil samples were stored away from light), and each sample was placed into a 50 mL centrifuge tube. Two minutes prior to the experiment, the prepared OFL solutions at concentrations of 1 mg/L and 10 mg/L were added to the centrifuge tubes according to a water-to-soil ratio of 25:1, and three centrifuge tubes constituted one experimental group. The mixture was then subjected to shaking incubation at 25 (±0.1) °C with a rotational speed of 180 r/min to ensure thorough contact between the solid and liquid phases and eliminate interference from external diffusion. At designated time points—specifically at 0.5, 1, 5, 15, 30, 60, 120, 180, 300, 420, 720, 1080, and 1440 min—the samples were collected to cover the three stages: rapid adsorption, slow adsorption, and adsorption equilibrium; immediately after sampling, the samples were filtered through a 0.22 μm water-based filter membrane to remove the adsorbent particles, thereby terminating the adsorption reaction. The supernatant obtained was used as the sample for HPLC analysis to determine the concentration of OFL (Figure 4).

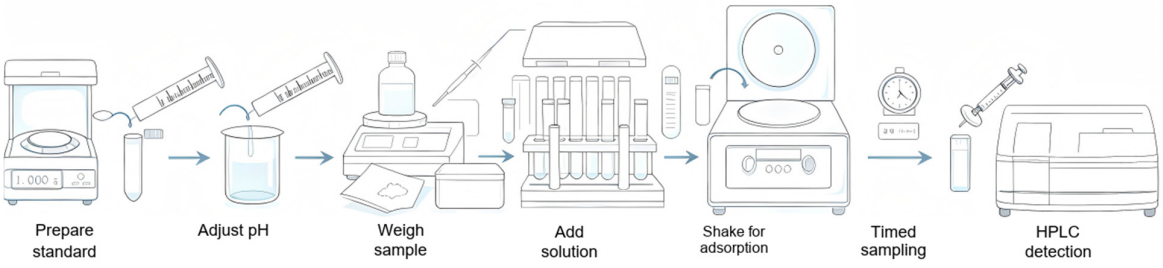


Figure 4. Flowchart of adsorption/desorption kinetic experiments.

After adsorption reached saturation, the mixture was centrifuged to remove the supernatant. Then, 50 mL of 0.01 mol·L^{-1} $CaCl_2$ solution free of the test drug was added. The mixture was placed in a dark water bath at (25 ± 1) °C with constant agitation at a speed of 180 r·min^{-1} for 1440 min. The supernatant was collected, centrifuged again, and filtered through a 0.22 μm filter membrane. The concentration of OFL in the supernatant was measured and the desorption amount was calculated.

3.2.3. Adsorption/Desorption Thermodynamic Experiment Design

Thermodynamic experiments were conducted based on the optimal conditions determined through kinetic studies. Prior to the experiment, gradient OFL solutions with concentrations of 0.1 mg/L, 0.2 mg/L, 0.5 mg/L, 10 mg/L, 1 mg/L, 20 mg/L, 40 mg/L, 60 mg/L, 80 mg/L, 100 mg/L, and 200 mg/L were prepared. Simultaneously, the pH of these solutions was adjusted to 6.0–7.0 using a 0.1 mol/L sodium hydroxide solution to ensure that the OFL was in its optimal adsorption form. A quantity of test soil samples (each weighing 1.2 g ± 0.01 g) was weighed and stored in the dark during the soil experiment. These samples were then placed in 50 mL centrifuge tubes. Two minutes prior to the experiment, according to a water-to-soil ratio of 25:1, three sets of centrifuge tubes were grouped together, and the prepared OFL solutions were added to the respective centrifuge tubes containing the soil samples. Three temperature gradients were established for the experiment: the first group consisted of temperatures of 25 °C, 35 °C, and 15 °C, used exclusively for the adsorption experiment; the second group consisted of temperatures of 5 °C, 15 °C, and 25 °C, used for the adsorption–desorption experiment. Temperature fluctuations were controlled within ±0.1 °C. The centrifuge tubes were placed in an oscillator, and the temperature was adjusted to 15, 25, or 35 °C, respectively. The oscillation speed remained identical to that used in the kinetic experiments, and the oscillation time was set to be no less than the kinetic equilibrium time, ensuring complete adsorption equilibrium at each temperature. After reaching equilibrium, samples were collected and filtered to determine the equilibrium concentration Ce (Figure 5).

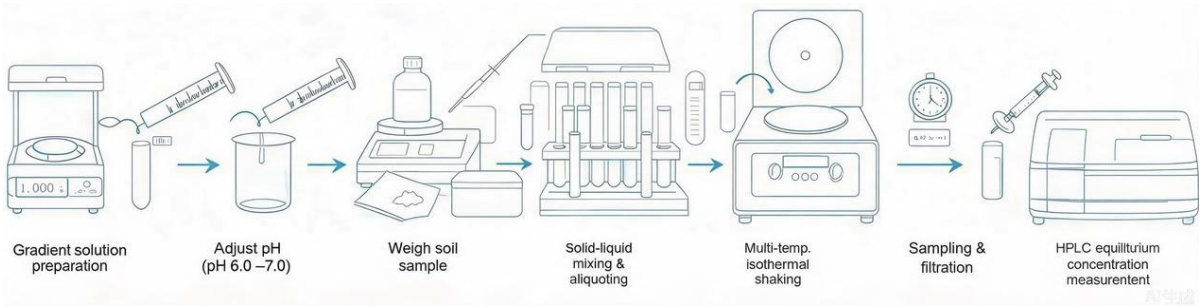


Figure 5. Thermodynamic test flowchart.

3.2.4. Influencing Factor Experimental Design

Building upon fundamental adsorption kinetic and thermodynamic experiments, single-factor experiments were conducted independently for pH, temperature, and coexisting cations. Each experimental group included three replicate samples and a blank control. All experiments were performed using a water-to-soil ratio of 25:1 and an oscillation speed of 180 r/min. The oscillation duration was set to 8 h, which corresponded to the equilibrium time determined by the kinetic analysis. Following the completion of the experiments, the samples were filtered through a 0.22 μm aqueous membrane filter, and the equilibrium concentration of OFL in the supernatant was measured via high-performance liquid chromatography (HPLC), from which the adsorption amount, desorption amount, and desorption rate were calculated.

(1) In the pH experiment, based on the natural pH range of the study area's sediments (7.5–8.5), a pH gradient covering acidic, neutral, and alkaline conditions (pH = 5, 7, and 9) was established. A 10 mg/L OFL solution was prepared, and its corresponding pH was adjusted using 0.1 mol/L HCl or 0.1 mol/L NaOH. After achieving adsorption equilibrium at a constant temperature of 25 °C, desorption tests were conducted using a 0.01 mol·L^{-1} $CaCl_2$ solution to investigate the intrinsic mechanism by which pH alters the dissociated

speciation of OFL and regulates the adsorption–desorption equilibrium via changes in the surface charge of the sediment.

(2) The coexisting-cation experiment selected typical cations of the watershed (Ca^{2+}, Mg^{2+}, and Na^{+}). Because the concentrations of these cations in arid-region surface waters are of the order of 10^{-3} to 10^{-2} mol L^{-1} rather than mg L^{-1}, the gradients are expressed in molar units: 0, 0.01, 0.05, and 0.1 mol L^{-1}, with an ion-free blank control (Table 3). The design deliberately separates two effects that are often conflated. First, the general ionic-strength (double-layer) effect is probed with the monovalent cation Na^{+}, which cannot compete strongly for specific surface sites. Second, specific cation competition is probed with the divalent cations Mg^{2+} and Ca^{2+}, which are compared directly; to make the comparison unambiguous, Mg^{2+} and Na^{+} were applied at the same molar concentration (0.01 mol L^{-1}), so that the difference between them isolates the contribution of specific competition from that of ionic strength, while Ca^{2+} was additionally applied at 0.05 and 0.1 mol L^{-1} so that its concentration dependence could be examined. An ion-OFL mixed reaction solution at a constant pH of 7.0 was prepared, and adsorption–desorption was carried out under otherwise identical conditions. By comparing the adsorption and desorption of OFL under different cation types and concentrations, this study separates specific cation competition from the general ionic-strength effect on the capacity of the sediment to sequester OFL.

Table 3. Parameter design table for influencing factors.

No.	Investigation Factor	Factorial Design	Other Conditions
(1)	Solution pH	5, 7, and 9 (acidic, neutral, and alkaline ranges)	25 °C; 10 mg L^{-1} OFL; adsorption followed by desorption in 0.01 mol L^{-1} $CaCl_2$
(2)	Reaction temperature	5, 15, and 25 °C(Group 2); 15, 25, and 35 °C (Group 1)	10 mg L^{-1} OFL; pH 7.0; adsorption (Group 1); adsorption and desorption (Group 2)
(3)	Type and concentration of coexisting cations	Na^{+}, Mg^{2+}, and Ca^{2+} at 0, 0.01, 0.05, and 0.1 mol L^{-1} (0 = blank control); Mg^{2+} and Na^{+} compared at matched molarity	pH 7.0 (constant); all other conditions identical to (1) and (2)
(4)	Initial OFL concentration (isotherms)	0.1, 0.2, 0.5, 1, 10, 20, 40, 60, 80, 100, and 200 mg L^{-1} (nominal)	5–35 °C; pH 6.0–7.0; 4–11 valid data points per temperature

(3) The temperature experiments followed the seasonal water temperature range of the Ili River Valley and were organized into two datasets. Group 2 used 5, 15, and 25 °C and comprised both adsorption and desorption isotherm experiments, whereas Group 1 used 15, 25, and 35 °C and comprised adsorption isotherm experiments only. A standardized 10 mg L^{-1} OFL solution at pH 7.0 was prepared, and the isotherm experiments were performed over the eleven nominal initial concentrations of 0.1, 0.2, 0.5, 1, 10, 20, 40, 60, 80, 100, and 200 mg L^{-1}, which yielded between 4 and 11 valid data points per temperature. The isothermal data were fitted by nonlinear regression with the Langmuir, Freundlich, and Dubinin–Radushkevich models, and the saturated adsorption capacity, adsorption constant, separation factor, 1/n value, and mean free energy of adsorption were compared in order to elucidate the effects of temperature on the adsorption capacity and the risk of desorptive release.

3.3. Analytical Methods

3.3.1. Adsorption Capacity and Desorption Capacity

The adsorption capacity is commonly used to evaluate the ability of an adsorbent to retain pollutants. The adsorption capacity of the sediments towards antibiotics was calculated with Equation (1) [47].

$$q_e = (C_0 - C_e)\, V/m \quad (1)$$

where q_e denotes the equilibrium adsorption capacity (mg kg^{-1});

C_0 denotes the initial concentration of the antibiotic in the solution before adsorption (mg L^{-1});

C_e denotes the concentration of the supernatant at equilibrium (mg L^{-1});

m denotes the mass of the adsorbent (kg); and

V represents the volume of the solution (L). With these units, Equation (1) gives q_e directly in mg kg^{-1}, which is the unit used throughout this paper.

Desorption is the reverse process of adsorption, and the desorption capacity describes the ability of the adsorbent to release the adsorbed species [47]:

$$q_d = (C_d - C_i)\, V/m \quad (2)$$

where q_d denotes the desorption amount (mg kg^{-1});

C_i denotes the initial concentration of the antibiotic in the desorption solution (mg L^{-1});

C_d denotes the concentration of the desorption equilibrium supernatant (mg L^{-1}). Other symbols are as defined above, and the same convention applies below.

3.3.2. Dynamic Equations Analysis

(1) Analysis using the pseudo-first-order kinetic equation (pseudo-first-order model).

The quasi-first-order kinetic model can be described by Equation (3) [48]:

$$dq_t/dt = k_1(q_e - q_t) \quad (3)$$

where q_t and q_e (mg kg^{-1}) represent the amounts of adsorbate on the adsorbent surface at time t and at equilibrium, respectively, and k_1 (min^{-1}) is the pseudo-first-order adsorption rate constant. With the boundary conditions $t = 0$, $q_t = 0$ and $t = t$, $q_t = q_t$, Equation (3) reduces to the linear form (4) [49]:

$$\ln(q_e - q_t) = \ln q_e - k_1 t \quad (4)$$

By plotting In(q_e–q_t) against t, if a straight line is obtained, this indicates that the adsorption mechanism follows a pseudo-first-order kinetic model. The pseudo-first-order kinetic parameter $k1$ and the theoretical equilibrium adsorption capacity q_e (i.e., q_e, cal) can be determined from the slope and intercept of the fitted straight line, respectively [49].

To determine whether the experimental data conform to the pseudo-first-order kinetic equation, it is necessary to know the equilibrium adsorption capacity q_e. However, in many cases, q_e is unknown. Furthermore, even when the variation of qt during the late adsorption stage has become quite slow. Its value may still be lower than the equilibrium adsorption capacity; indeed, in many instances, the pseudo-first-order kinetic equation fails to adequately describe the experimental data over the entire time range [50]. In this study, when performing a pseudo-first-order kinetic fit on the kinetic data, the experimental value of q_t—which remains nearly constant during the late adsorption stage—is used as the equilibrium adsorption capacity (q_e, exp). If the adsorption process follows the pseudo-first-

order kinetic equation, the calculated value of q_e should equal or closely approximate the experimental value of q_e. Otherwise, even if the correlation coefficient R^2 from the linear fitting of the pseudo-first-order kinetic equation is high, the equation cannot be employed to characterize the adsorption process [50].

(2) Analysis of the pseudo-second-order adsorption kinetic equation.

The quasi-second-order kinetics model can be described by Equation (5) [51]:

$$dq_t/dt = k_2(q_e - q_t)^2 \quad (5)$$

where q_e and q_t are as defined above and k_2 (kg mg^{-1} min^{-1}) is the pseudo-second-order adsorption rate constant. Applying the boundary conditions $t = 0$, $q_t = 0$ and $t = t$, $q_t = q_t$ and separating the variables, Equation (5) reduces to the linear form (6) [51]:

$$t/q_t = t/q_e + 1/(k_2 {q_e}^2) \quad (6)$$

By plotting t against t/q, if a straight line is obtained, this indicates that the adsorption mechanism follows a pseudo-second-order kinetic model. Based on the slope and intercept of the fitted straight line, the theoretical equilibrium adsorption capacity *qe* (i.e., *qe*, cal) and the pseudo-second-order kinetic rate constant k_2 can be calculated, respectively [51].

When t tends to 0, the initial adsorption rate h (mg kg^{-1} min^{-1}) can be calculated using Equation (7):

$$h = k_2 {q_e}^2 \quad (7)$$

Furthermore, using Equation (8), the time $t_{1/2}$ (min) required for the adsorption amount to reach half of the equilibrium adsorption amount can be derived:

$$t_{1/2} = 1/(k_2 q_e) \quad (8)$$

The larger the values of h and k_2, the faster the adsorption rate. Compared with the pseudo-first-order kinetic model, the pseudo-second-order model is more effective at elucidating the behavior of the entire adsorption process and aligns better with the rate-determining step [52].

(3) Intra-particle diffusion equation analysis (intra-particle diffusion model).

The particle internal diffusion model can be simply expressed using Equation (9) [53]:

$$q_t = k_d t^{1/2} + I \quad (9)$$

where q_t has the same meaning as above, k_d (mg kg^{-1} min$^{-1/2}$) is the intraparticle diffusion rate constant, and I (mg kg^{-1}) is a parameter indicating the thickness of the boundary liquid film surrounding the particle, with a larger value of I corresponding to a thicker boundary liquid film [54].

When plotting qt against $t^{1/2}$, if a straight line is obtained, this indicates that the adsorption process involves diffusion of the adsorbate within the adsorbent particle. If this straight line passes through the origin, this suggests that intra-particle diffusion is the sole limiting step in determining the adsorption rate. However, if the straight line does not pass through the origin, this indicates that intra-particle diffusion is not the sole limiting step in the adsorption process and that the process may also involve other steps, such as diffusion through the surface liquid film layer (i.e., the transport of the adsorbate outside the particle) [55].

Generally, when plotting qt against $t^{1/2}$, a curve divided into three distinct segments can be obtained: the two ends of the curve exhibit curvature, while the middle segment is linear. These segments correspond to the three steps of the adsorption process. The first

segment of the curve reflects the transfer process of the adsorbate from outside the particle; during this stage, the adsorption rate is controlled by the diffusion rate of the adsorbate within the surface liquid film layer. The middle linear segment of the curve results from the diffusion of the adsorbate within the particle; during this stage, the adsorption rate is governed by the diffusion rate of the adsorbate within the particle [56]. The third segment of the curve represents the final equilibrium stage, during which the diffusion of the adsorbate within the particle gradually slows down due to factors such as the progressive reduction of pore sizes within the particle, the continuous increase in electrostatic repulsive forces, or the decrease in the concentration of the adsorbate outside the particle. These three segments of the diffusion curve may not always appear in every adsorption experiment; depending on the timing of the initial sampling, the first segment may be absent if samples were not collected promptly, and the third segment may also vary depending on the timing of the final sampling point.

(4) Elovich Equation Analysis

The Elovich model can effectively describe the behavior of pollutants on heterogeneous solid adsorption surfaces. This model does not assume any specific mechanism between the adsorbate and the adsorbent. It provides a good description of the kinetic adsorption process and reveals data irregularities that may be overlooked by other kinetic equations. It is applicable to reaction processes with relatively high activation energies. The expression for this model is an empirical formula, as shown in Equation (10) [57].

$$q_t = (1/beta)\ \ln(alpha\ beta) + (1/beta)\ \ln t = a + b\ \ln t \quad (10)$$

where $a = (1/beta)\ \ln(alpha\ beta)$ is the intercept (mg kg^{-1}) and $b = 1/beta$ is the slope (mg kg^{-1}); *alpha* is the initial adsorption rate constant (mg kg^{-1} min^{-1}) and *beta* is the desorption constant (kg mg^{-1}). The earlier statement that a is itself the initial adsorption rate was incorrect and has been corrected.

The larger the value of *alpha* (equivalently, the larger the intercept a) and the smaller the value of *beta* (equivalently, the larger the slope b), the stronger the adsorption effect. Because Equation (10) is linear in its parameters, the linearized and nonlinear regressions are mathematically identical for this model, and both were confirmed to return the same coefficients and the same coefficient of determination; the fitted lines in (Figure 7c,d) are therefore plotted against ln t, as Equation (10) requires, and not against t. If a straight line is observed, the Elovich model can be used to describe the adsorption process.

3.3.3. Thermodynamic Equation Analysis

(1) Langmuir isotherm analysis

For ideal monolayer adsorption, the Langmuir adsorption isotherm equation can be expressed as [58]

$$q_e = q_m K_L C_e/(1 + K_L C_e) \quad (11)$$

where C_e (mg L^{-1}) denotes the residual concentration of the adsorbate in the solution at adsorption equilibrium, q_e (mg kg^{-1}) represents the amount of adsorbate adsorbed on the adsorbent surface at adsorption equilibrium, q_m (mg kg^{-1}) is the adsorption capacity when the entire surface area of the adsorbent is covered by a monolayer of the adsorbate (the saturated adsorption capacity), and K_L (L mg^{-1}) is the Langmuir adsorption constant, which reflects the affinity of the binding sites and depends on the temperature and adsorption enthalpy [59].

By rearranging Equation (11), we obtain the linear form of the Langmuir isotherm [60]:

$$1/q_e = 1/(K_L q_m C_e) + 1/q_m \quad (12)$$

By plotting $1/q_e$ against $1/C$, if a straight line is obtained, this indicates that the adsorption follows the Langmuir adsorption isotherm model. The values of kL and qm can then be determined from the slope and intercept of the fitted straight line respectively.

In the Langmuir isotherm model, a dimensionless constant—namely, the separation factor (or equilibrium coefficient) Rz—is commonly used to describe its fundamental characteristics. The calculation formula for RL is given by [60]

$$R_L = 1/(1 + K_L C_0) \quad (13)$$

where K_L (L mg^{-1}) is the Langmuir adsorption constant and C_0 (mg L^{-1}) is the series of initial concentrations of the adsorbate used in the isotherm experiment. The parameter R_L reflects the characteristics of the isotherm and the adsorption process. If $R_L = 0$, the adsorption is irreversible; if $0 < R_L < 1$, the adsorption is favorable, indicating that the adsorbate can readily be taken up by the adsorbent within the experimental concentration range; if $R_L = 1$, the adsorption is linear and reversible; and if $R_L > 1$, the adsorption is unfavorable and therefore difficult to achieve.

(2) Freundlich isotherm analysis

When the adsorbent surface is heterogeneous, when the adsorption equilibrium constant depends on the surface coverage, or when describing the adsorption of high-concentration adsorbates, the Freundlich adsorption isotherm model can be applied. Its expression is given by [60]

$$q_e = K_F C_e^{1/n} \quad (14)$$

where q_e and C_e have the same meanings as before and K_F and n are the Freundlich adsorption constants. The constant K_F reflects the adsorption capacity and is influenced by the properties of the adsorbate and the adsorbent, their respective amounts, and the temperature; a larger K_F indicates a stronger bonding force between the adsorbent and the adsorbate [57]. The constant n is the nonlinear factor or potential inhomogeneity factor and reflects the heterogeneity of the adsorption surface. Because n appears as a reciprocal exponent, the Freundlich model requires $n > 0$ for the isotherm to be physically valid: a negative or zero value of n is not admissible since it would imply that the adsorbed amount decreases with increasing concentration, which contradicts the nature of adsorption. The magnitude of $1/n$ indicates the ease of the adsorption process: when $0.1 < 1/n < 0.5$, the adsorption is facile, and when $1/n > 2$, it is difficult. When $1/n = 1$, the isotherm is linear and has the character of a partition coefficient. The constants K_F and $1/n$ can be used to compare the characteristics of different adsorbents. It should be emphasized that the Freundlich model is an empirical description of adsorption on a heterogeneous surface and does not by itself assume either monolayer or multilayer coverage.

Equation (14) is often transformed into a double-logarithmic form to obtain K_F and $1/n$; taking the logarithm of both sides of Equation (14) gives Equation (15). In this work, however, the parameters of Equations (11) and (14) were obtained by nonlinear regression on the untransformed isotherm (Section 3.3.4), and the linearized form (15) was used only as a diagnostic because linearizing these equations distorts the error structure and can return physically meaningless parameters (Section 4.1):

$$\ln q_e = (1/n) \ln C_e + \ln K_F \quad (15)$$

By plotting ln q versus ln C_e, if a straight line is obtained, this indicates that the adsorption follows the Freundlich adsorption isotherm model. The values of 1/n and k_F can be determined separately based on the slope and intercept of the fitted straight line, respectively [60].

3.3.4. Nonlinear Regression and Complementary Analyses

The linearized forms (Equations (4), (6), (12) and (15)) were retained only for diagnostic comparison because linearization weights the transformed residuals rather than the measured quantities. For the pseudo-second-order model, for example, the linearized form is dominated by the late-time points, at which qt is nearly constant, and it can therefore return $R^2 > 0.99$ in the transformed space while the same coefficients reproduce the measured qt poorly (Section 4.1). All parameters are quoted with the standard error obtained from the covariance matrix, and 95% confidence intervals were obtained from the t distribution.

Because R^2 alone is not a sufficient criterion of model adequacy, several complementary statistics are reported for every fit: the coefficient of determination R^2, adjusted R^2 (which penalizes additional parameters), root-mean-square error (RMSE), reduced chi-square, and Akaike information criterion AIC = $n\ ln(SSres/n) + 2p$, where n is the number of data points and p is the number of fitted parameters. When two models have different numbers of parameters, the model with the lower AIC is preferred, and a difference of less than about 2 indicates that the two models are statistically indistinguishable.

The Boyd model was used to discriminate film diffusion from intraparticle diffusion as the rate-limiting step. The fractional approach to equilibrium $F = q_t/q_e$ is converted into the function Bt, and Bt is plotted against t according to Equation (16). A straight line through the origin indicates that intraparticle diffusion controls the rate, whereas a non-zero intercept indicates a contribution from film diffusion. The significance of the intercept was tested with a t test at the 95% level since extrapolating a line to t = 0 without a significance test does not by itself establish that the intercept differs from zero.

$$Bt = -0.4977 - ln(1 - F)\ (F \geq 0.85) \tag{16}$$

The Dubinin–Radushkevich (D-R) isotherm was applied as an independent check on the nature of the uptake because the mean free energy E derived from it distinguishes physisorption from chemisorption; the equations are given in (17) and (18), where epsilon is the Polanyi potential, R the gas constant, T the absolute temperature, and q_s the D-R saturation capacity. A value of E below about 8 kJ mol^{-1} indicates physisorption, whereas a value above about 8 kJ mol^{-1} indicates chemisorption or ion exchange.

$$q_e = q_s\ exp(\text{-}KDR\ epsilon2),\ epsilon = RT\ ln(1 + 1/Ce) \tag{17}$$

$$E = 1/(2\ KDR)\text{^}0.5 \tag{18}$$

Adsorption thermodynamics were evaluated from the temperature dependence of the Langmuir constant with the van't Hoff relation (19), with the Gibbs energy given by (20). Here, $K0$ is the dimensionless equilibrium constant obtained from KL as $K0$ = KL × MOFL × 1000, with MOFL = 361.37 g mol^{-1}; $dH0$ and $dS0$ were obtained from the slope and intercept of ln $K0$ against $1/T$, and $dG0$ at each temperature from $dG0 = dH0 - T\ dS0$. The sign of dH0 indicates whether adsorption is endothermic or exothermic, and the sign of $dG0$ indicates whether it is spontaneous.

$$ln\ K0 = -dH0/(RT) + dS0/R \tag{19}$$

$$dG0 = -RT\ ln\ K0 = dH0 - T\ dS0 \tag{20}$$

Finally, the linear partition coefficient Kd (L kg^{-1}) was obtained by regression of qe on Ce constrained through the origin, and the hysteresis index H was calculated from the Freundlich exponents of the adsorption (na) and desorption (nd) branches as

$H = (1/nd - 1/na)/(1/nd)$; $H > 0$ indicates that the desorption branch lies above the adsorption branch, i.e., that hysteresis occurs.

4. Results and Analysis

4.1. Adsorption Kinetics of Calcium Carbonate Precipitates on OFL

For calcium-rich sediments from a sewage discharge outlet on the Ili River, the adsorption curve of OFL and the fits of the adsorption kinetic models indicate a two-stage process consisting of a fast stage and a slow equilibrium stage. For the XFD series, the first sampling point (0.5 min) already corresponds to 70.1% (1 mg L^{-1}) and 71.5% (10 mg L^{-1}) of the plateau value, and the whole series has leveled off by 8 h; for the second 1 mg L^{-1} series (samples 237–347), the first point corresponds to 84.6% of the plateau. Most of the uptake therefore occurs faster than the sampling resolution, which is why the rate constants of the classical rate laws are poorly constrained by these data.

As the initial concentration of the solution increases, the equilibrium adsorption capacity of the sediment also increases. For the XFD series, the mean plateau adsorption capacities at $t \geq 180$ min were 15.09 and 135.35 mg kg^{-1}, respectively, so the equilibrium adsorption capacity is positively correlated with the initial OFL concentration.

To characterize the adsorption of OFL on the calcium-bearing sediments, the pseudo-first-order (PFO), pseudo-second-order (PSO), intraparticle diffusion (IPD), and Elovich models were fitted to the data by nonlinear regression on the original q-t scale (Section 3.3.4); the results are shown in Figures 6 and 7 and Table 4. Panels (a) and (b) of Figure 6 show that the PFO model does not describe either dataset: it can represent the initial uptake but not the slow drift of qt that continues after the first few minutes, giving $R^2 = 0.372$ (1 mg L^{-1}) and 0.201 (10 mg L^{-1}). Panels (c) and (d) show the same behavior for the PSO model ($R^2 = 0.533$ and 0.319). The fitted rate constants are consequently very large (k1 = 2.24 and 2.31 min^{-1}; k2 = 0.289 and 0.0318 kg mg^{-1} min^{-1}) and the corresponding half-times are only 0.24 min (Table 4), i.e., these models describe an essentially instantaneous step that the data cannot resolve. By contrast, the Elovich model, which represents the slow redistribution of the adsorbate over a heterogeneous surface with an exponentially decaying rate, reproduces both datasets much better ($R^2 = 0.829$ and 0.589) and has the lowest AIC of the three models (Table 4). On this evidence, the adsorption of OFL on these sediments is not adequately described by a single-site rate law, and the previously reported excellent fit of the PSO model reflects the use of its linearized form rather than the data themselves.

To make the point explicit, the linearized forms of the two models were also fitted for comparison (the rows marked linearized in Table 4). The linearized PSO fit (t/qt versus t) gives $R^2 = 0.9944$, 0.9881, and 0.9998 for the 1 mg L^{-1} XFD series, the 10 mg L^{-1} series, and the 237–347 series, respectively, which is why the original submission reported $R^2 > 0.98$ and concluded that the PSO model describes the process; yet, when the same coefficients are substituted back into the model and compared with the measured qt, the coefficients of determination are −5.32, −4.28, and −12.00. The linearized PFO form is even more problematic: because $\ln(qe - qt)$ is undefined once qt exceeds the chosen qe, it can only be computed by discarding the late-stage points, and the surviving subset is biased towards the early stage. This is precisely the origin of the negative k1 values (−0.0031 and −0.00157 min^{-1}) reported in the original Table 4 and the negative k1 values (−0.00045 and −0.00185 min^{-1}) reported in the original Table 5: the least-squares slope is dominated by the scatter in the residual term $(qe - qt)$ wherever the assumed qe is smaller than some of the measured qt, so the slope of $\ln(qe - qt)$ against t becomes positive and k1 acquires a negative sign. A negative rate constant is physically meaningless; in this dataset, it is a symptom of an inappropriate fitting procedure rather than of the data, and all parameters reported in

Table 4 were therefore obtained by nonlinear regression, in which the rate constants are constrained to be positive.

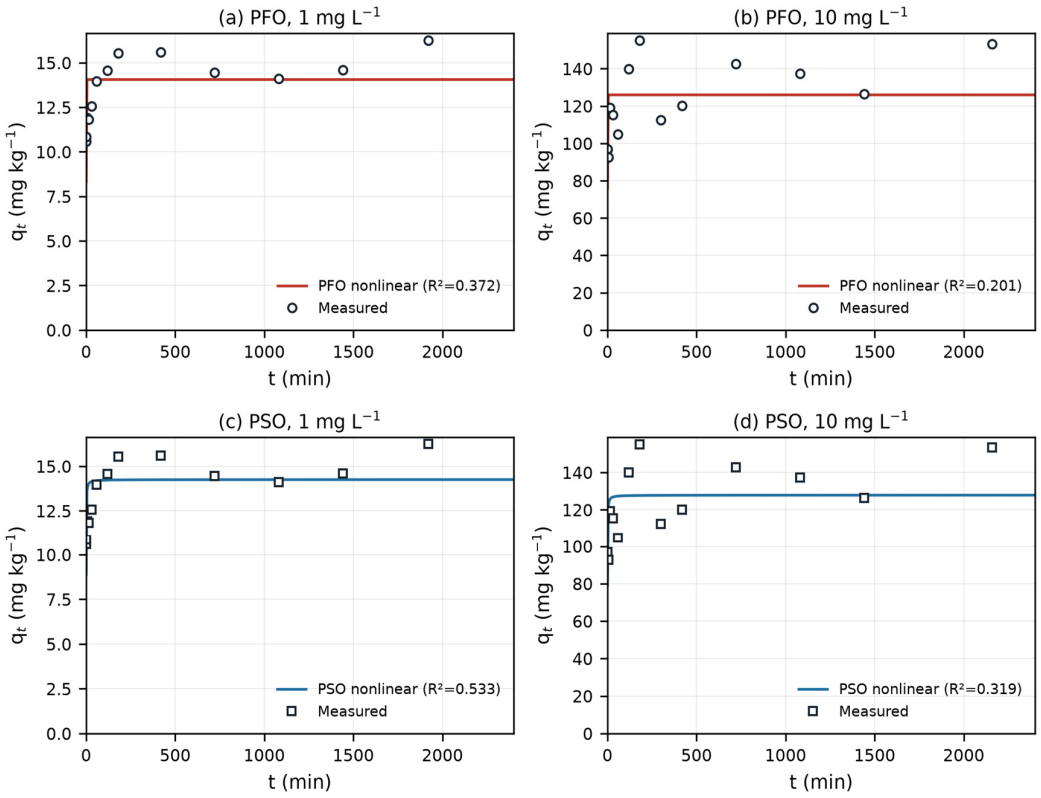


Figure 6. Adsorption kinetics of OFL on the sediments at 1 and 10 mg L^{-1}, with nonlinear least-squares fits of the pseudo-first-order and pseudo-second-order models. (**a**) Pseudo-first-order, 1 mg L^{-1}; (**b**) pseudo-first-order, 10 mg L^{-1}; (**c**) pseudo-second-order, 1 mg L^{-1}; (**d**) pseudo-second-order, 10 mg L^{-1}. Symbols are measured values and lines are the nonlinear fits.

The Boyd model was used to test the diffusion interpretation quantitatively (Table 4). For the 1 mg L^{-1} XFD series, $Bt = 2.63 \times 10^{-3}$ t + 1.795 with $R^2 = 0.237$; the intercept is not significantly different from zero (t = 1.64, below the 95% critical value), so intraparticle diffusion controls the rate for this dataset. The same result is obtained for the 10 mg L^{-1} series ($Bt = 3.07 \times 10^{-3}$ t + 2.189, $R^2 = 0.257$, intercept $t = 1.84$, not significant) and the desorption data (intercept −0.010, $t = -0.02$). For the second 1 mg L^{-1} series (samples 237–347), however, the intercept is significantly different from zero ($Bt = 1.26 \times 10^{-3}$ t + 4.861, t = 4.48 > tcrit), so film diffusion also contributes to rate control in that experiment.

The intraparticle diffusion plots are shown in Figure 7a,b and the fitted segment parameters are listed in Table 4. For the 1 mg L^{-1} XFD series, the data fall on three segments: an initial steep segment (kp1 = 0.866, R^2 = 1.000) that reflects rapid surface uptake, a second segment (kp2 = 0.379, R^2 = 0.968), and a final, nearly flat segment (kp3 = 0.023, R^2 = 0.056) that corresponds to the approach to equilibrium. None of the segments passes through the origin and the extrapolated intercepts increase from C1 = 9.98 to C3 = 14.25 mg kg^{-1}, which indicates that boundary-layer (film) diffusion contributes to rate control. The 10 mg L^{-1} series behaves differently: its first segment has a negative slope (kp1 = −2.87) because these data are markedly scattered and the three points assigned to that segment do not define a decreasing qt with increasing t1/2. The second and third segments of the 10 mg L^{-1} series have positive slopes (kp2 = 4.22 and kp3 = 1.08), but the fits are poor (R^2 = 0.663 and 0.606). Taken together, the IPD analysis shows that intraparticle diffusion is not the sole rate-limiting step, but these data are too scattered to resolve the individual diffusion stages for the 10 mg L^{-1} treatment.

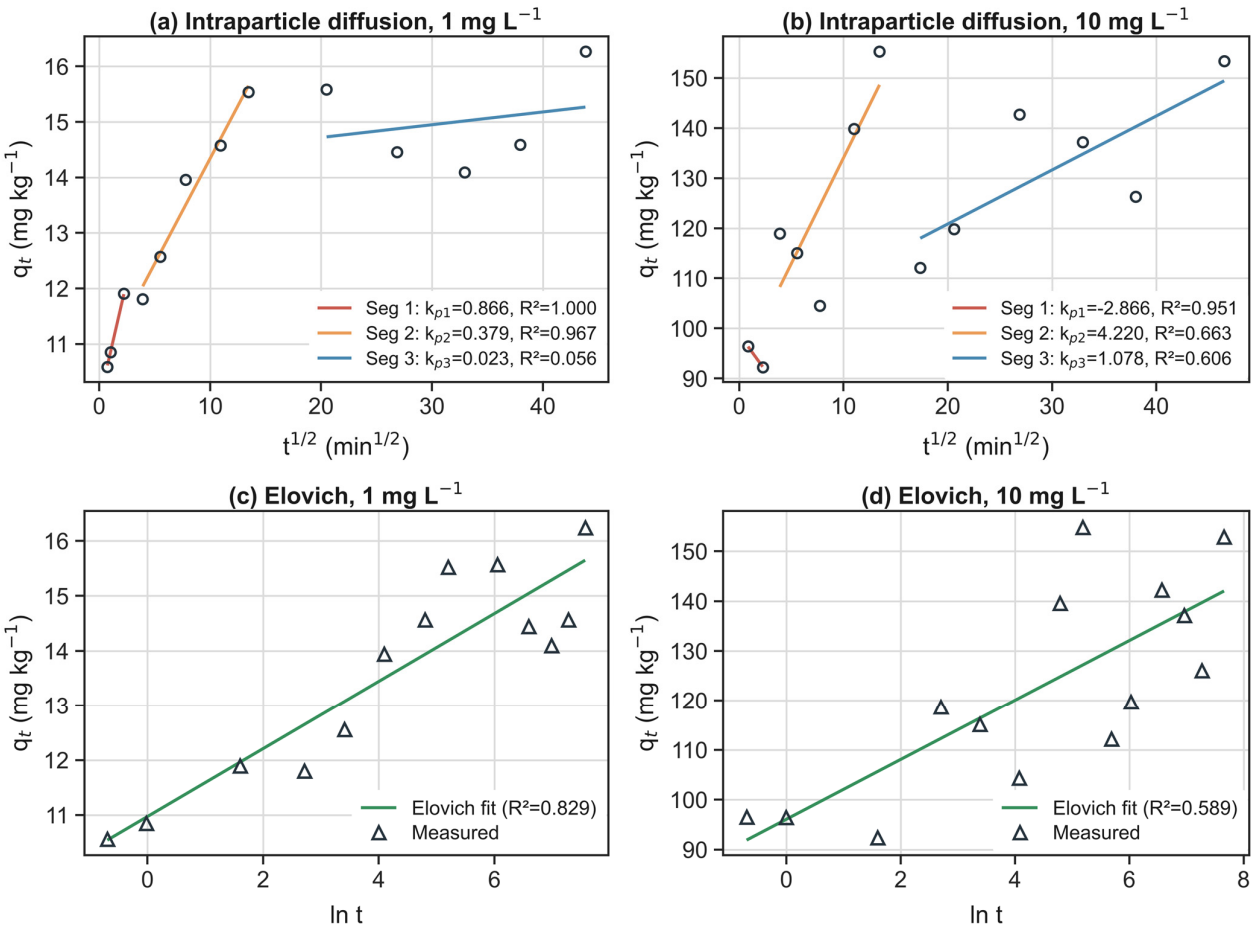


Figure 7. Intraparticle diffusion and Elovich analyses of the OFL adsorption kinetics. (**a**) intraparticle diffusion, 1 mg L^{-1}; (**b**) intraparticle diffusion, 10 mg L^{-1}; (**c**) Elovich, 1 mg L^{-1}; (**d**) Elovich, 10 mg L^{-1}.

The Elovich model describes adsorption on a heterogeneous surface for which the activation energy increases with coverage, and it gave the best fit of the four models for both XFD datasets (Table 4). Its parameters are the intercept a = 10.95 (1 mg L^{-1}) and 96.09 (10 mg L^{-1}) mg kg^{-1} and the slope b = 0.6198 ± 0.221 and 5.994 ± 0.040 mg kg^{-1}; the slope is determined precisely while the intercept is correlated with the scatter of the earliest points. Because Equation (10) is linear in a and b, the nonlinear and linearized regressions are mathematically identical and give the same coefficient of determination (0.829 and 0.589), so no linearization artefact arises for this model. The fitted lines are plotted against ln t in Figure 7c,d, as required by Equation (10). The improvement of the Elovich model over PFO and PSO indicates that the adsorption energy is distributed over a range of sites rather than being a single-valued constant, which argues against interpreting the kinetics in terms of one chemical rate-determining step. This result differs from the conclusion of Zhang R et al. [41], who reported pseudo-second-order control for a comparable system; the difference is attributable to the fitting method because a linearized PSO fit also gives $R^2 > 0.99$ for our data.

Table 4. Nonlinear kinetic fitting parameters for the adsorption of OFL on the sediments at 25 °C.

Kinetic Model	Parameter	1 mg L^{-1} (XFD-1; C_0 = 1.27 mg L^{-1})	10 mg L^{-1} (XFD-10; C_0 = 11.48 mg L^{-1})
PFO (nonlinear)	$q_{e,cal}$ (mg kg^{-1})	14.06 ± 0.46	125.97 ± 5.56
	k_1 (min^{-1})	2.24 ± 0.59	2.31 ± 0.87
	R^2/adj-R^2	0.372/0.315	0.201/0.134
	RMSE/chi^2/AIC	1.42/1.93/13.10	17.95/36.46/84.86
PFO (linearized, $\ln(q_e - q_t)$ vs. t)	k_1 (min^{-1})	1.13×10^{-3}	8.70×10^{-4}
	$q_{e,cal}$ (mg kg^{-1})	15.42	144.64
	R^2	0.471	0.612
PSO (nonlinear)	$q_{e,cal}$ (mg kg^{-1})	14.26 ± 0.41	127.85 ± 5.32
	k_2 (kg mg^{-1} min^{-1})	0.289 ± 0.109	0.0318 ± 0.0178
	$h = k_2 q_e^2$ (mg kg^{-1} min^{-1})	58.8	519.9
	$t_{1/2}$ (min)	0.243	0.246
	R^2/adj-R^2	0.533/0.490	0.319/0.262
	RMSE/chi^2/AIC	1.22/1.42/9.26	16.58/30.99/82.62
PSO (linearized, t/q_t vs. t)	$q_{e,cal}$ (mg kg^{-1})	15.42	144.64
	k_2 (kg mg^{-1} min^{-1})	5.53×10^{-3}	2.70×10^{-4}
	R^2	0.9944	0.9881
	R^2 on the original q-t scale	−5.32	−4.28
IPD (3 segments)	$k_{p1}/C_1/R^2$	0.866/9.98/1.000	−2.87 (a)/99.22/0.951
	$k_{p2}/C_2/R^2$	0.379/10.55/0.968	4.22/91.88/0.663
	$k_{p3}/C_3/R^2$	0.023/14.25/0.056	1.08/99.38/0.606
Elovich	a (mg kg^{-1})	10.95	96.09
	b (mg kg^{-1})	0.6198 ± 0.221	5.994 ± 0.040
	R^2/adj-R^2/RMSE/AIC	0.829/0.814/0.740/−3.82	0.589/0.555/12.87/75.53
Boyd	slope B (min^{-1})	2.63×10^{-3}	3.07×10^{-3}
	intercept/R^2	1.795/0.237	2.189/0.257
	intercept t statistic	1.64	1.84

Table 5. Nonlinear kinetic fitting parameters for the adsorption and desorption of OFL at 1 mg L^{-1}.

Kinetic Model	Parameter	Adsorption (1 mg L^{-1}; Samples 237–347; C_0 = 1.20 mg L^{-1})	Desorption (1 mg L^{-1}; 0.01 mol L^{-1} $CaCl_2$; V/m = 41.67 L kg^{-1})
PFO (nonlinear)	$q_{e,cal}$ (mg kg^{-1})	22.62 ± 0.21	3.86 ± 0.29
	k_1 (min^{-1})	3.62 ± 0.38	0.113 ± 0.057
	R^2/adj-R^2	0.688/0.660	0.409/0.355
	RMSE/chi^2/AIC	0.64/0.24/−7.53	0.79/16.16/−2.08
PFO (linearized)	k_1 (min^{-1})	1.90×10^{-3}	7.41×10^{-3}
	R^2	0.419	0.827
PSO (nonlinear)	$q_{e,cal}$ (mg kg^{-1})	22.72 ± 0.22	3.92 ± 0.26
	k_2 (kg mg^{-1} min^{-1})	0.534 ± 0.134	0.0757 ± 0.0444
	h (mg kg^{-1} min^{-1})	275.5	1.16
	$t_{1/2}$ (min)	0.082	3.37
	R^2/adj-R^2	0.659/0.628	0.594/0.557
	RMSE/chi^2/AIC	0.67/0.26/−6.37	0.66/4.62/−6.97
PSO (linearized)	R^2	0.9998	0.9957
	R^2 on the original q-t scale	−12.00	0.462
IPD (3 segments)	$k_{p1}/C_1/R^2$	2.44/18.08/0.871	0.174/1.597/0.934
	$k_{p2}/C_2/R^2$	−0.064 (a)/23.02/0.070	0.148/1.938/0.985
	$k_{p3}/C_3/R^2$	−0.017 (a)/23.14/0.128	0.035/3.319/0.372
Elovich	a (mg kg^{-1})	21.31	1.642
	b (mg kg^{-1})	0.2378 ± 0.0566	0.3975 ± 0.213
	R^2/adj-R^2/RMSE/AIC	0.266/0.200/0.984/3.59	0.929/0.922/0.275/−29.60
Boyd	intercept/t statistic	4.861/4.48	−0.010/−0.02

As shown in Table 4, the nonlinear PSO fit is poor for both XFD datasets. The two-stage shape of the adsorption curves, with 70–85% of the plateau reached at the first sampling point and a much slower subsequent drift, is better explained by a fast, largely non-specific uptake onto accessible surface and near-surface sites followed by a slow redistribution or surface-complexation step that has a broad distribution of activation energies, the picture described by the Elovich model. Direct evidence for chemical bonding, such as FTIR or XPS spectra recorded before and after adsorption, or activation energy from an Arrhenius analysis, was not obtained in this study, and the Dubinin–Radushkevich analysis (Section 4.3) in fact points to physisorption-dominated uptake (E = 0.08–0.25 kJ mol^{-1}). The mechanism is therefore described in Section 5 as chemisorption-influenced rather than chemically rate-controlled, in line with the request in the review that the claim should be supported by independent evidence.

4.2. Desorption Kinetic Behavior of Calcium Deposits on OFL

Figure 8 shows the desorption curves of OFL from the Ili River basin sediments, together with the fits of the four kinetic models, for the second 1 mg L^{-1} series (samples 237–347) that had first been loaded with OFL. Desorption was carried out with 50 mL of 0.01 mol L^{-1} $CaCl_2$, giving a liquid-to-solid ratio of 41.67 L kg^{-1}.

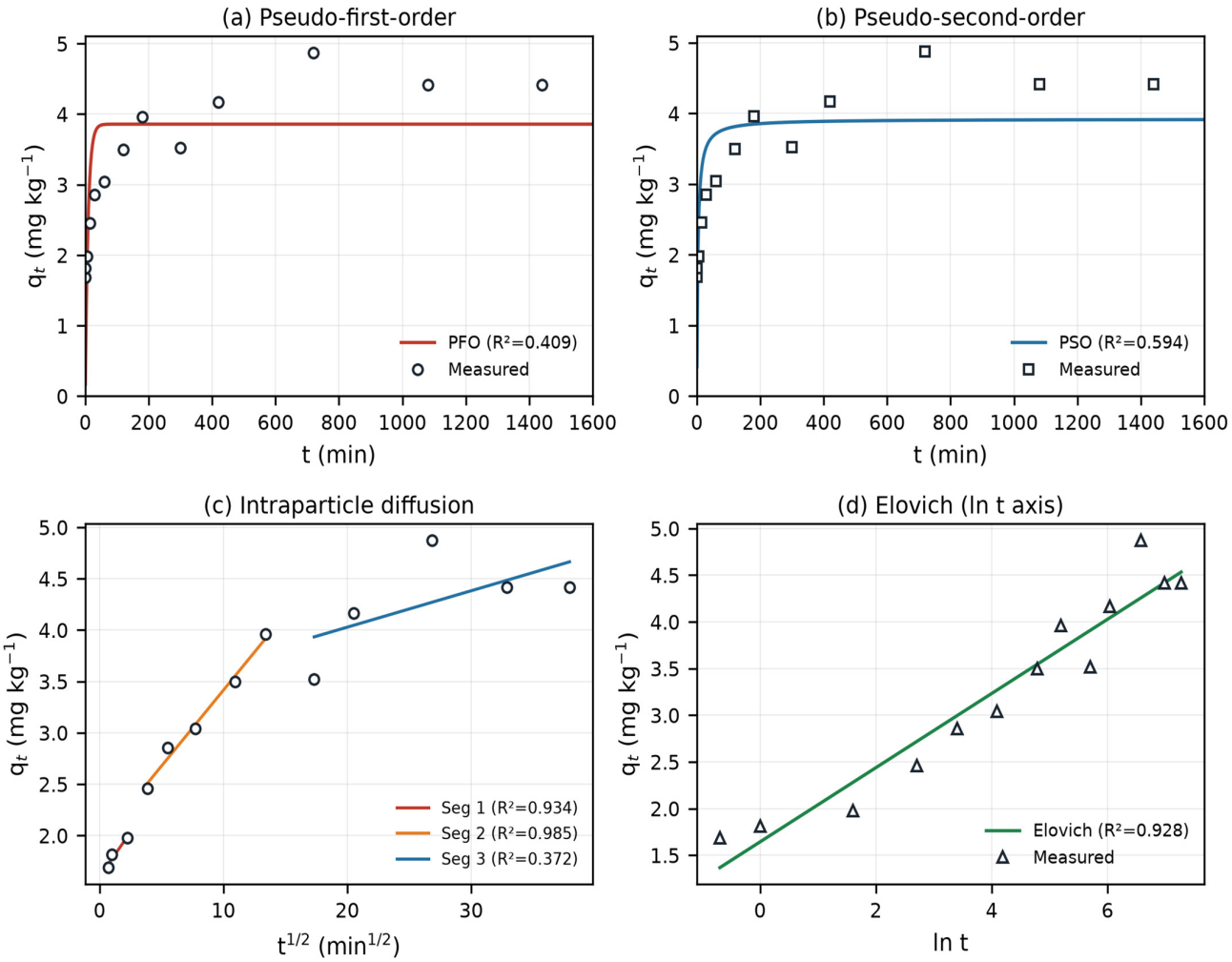


Figure 8. Desorption kinetics of OFL at 1 mg L^{-1}. (**a**) Pseudo-first-order; (**b**) pseudo-second-order; (**c**) intraparticle diffusion; (**d**) Elovich.

To characterize the desorption of OFL, the same four models were fitted by nonlinear regression; the results are shown in Figure 8 and Table 5. Panels (a)–(d) of Figure 8 give the PFO, PSO, IPD, and Elovich fits, respectively, all drawn on a common time axis. The PFO model underestimates the measured desorption (R^2 = 0.409, fitted equilibrium 3.86 mg kg^{-1} against a measured plateau of 4.23 mg kg^{-1}) and, as for adsorption, cannot represent the late-stage drift. The PSO model is better but still incomplete (R^2 = 0.594, fitted equilibrium 3.92 mg kg^{-1}), and its linearized form again reports R^2 = 0.9957 in the transformed space while giving R^2 = 0.462 on the original scale (Table 5).

The Elovich model provides by far the best description of desorption (R^2 = 0.929, adjusted R^2 = 0.922, RMSE = 0.275 mg kg^{-1}, AIC = −29.60) and is the only model whose residuals show no systematic trend (Figure 8d); the fitted slope is b = 0.397 ± 0.213 mg kg^{-1} and the intercept is a = 1.642 mg kg^{-1}. The superiority of the Elovich model for desorption, as for adsorption, indicates that release is governed by a distribution of site energies rather than by a single chemical desorption step, which is the expected signature of a clay-carbonate assemblage in which OFL is bound at sites of differing accessibility. The half-time derived from the PSO fit for desorption is t1/2 = 3.37 min, which again reflects the fact that most of the release occurs within the first sampling interval: 39.9% of the final desorbed amount is already present at 0.5 min.

Comparison of the desorption parameters with those of the corresponding adsorption experiment (Table 5) shows that the two branches are not interchangeable: the adsorption experiment on the 237–347 series gave qe = 22.62 mg kg^{-1} with k_2 = 0.534 kg mg^{-1} min^{-1}, whereas desorption gave qe = 3.92 mg kg^{-1} with k_2 = 0.0757 kg mg^{-1} min^{-1}, and the best-fitting model differs between the two directions. The original Table 5 listed 0.0378 mg kg^{-1} and 0.07577 as the equilibrium capacities of the adsorption and desorption branches respectively; these two numbers are in fact the PSO rate constant and the equilibrium capacity of the desorption branch, i.e., they were transposed, and the value quoted for the adsorption branch was inconsistent with the measured concentrations by more than two orders of magnitude. The corrected values are given in Table 5. The reason why the two 1 mg L^{-1} experiments in the original Tables 4 and 5 differed by an order of magnitude is now also clear: they are different sediment series (XFD-1 and samples 237–347, collected at different sampling points) and therefore differ in capacity, and the two datasets are labeled explicitly in Tables 4 and 5. The desorption process can still be divided into two stages, a rapid release from easily accessible sites and a slow approach to equilibrium controlled by the more strongly bound fraction.

The IPD plots for desorption (Figure 8c and Table 5) also consist of three segments, with decreasing slopes (kp1 = 0.174, kp2 = 0.148, and kp3 = 0.035) and increasing intercepts (C1 = 1.60 to C3 = 3.32 mg kg^{-1}). None of the segments passes through the origin, so intraparticle diffusion is not the sole rate-limiting step in desorption; the Boyd analysis reaches the same conclusion, giving an intercept that is statistically indistinguishable from zero (t = −0.02), so the desorption rate is likewise dominated by particle diffusion. The apparent discrepancy between the IPD intercepts, which suggest a boundary-layer contribution, and the Boyd result, which does not, reflects the fact that the IPD intercept C is an extrapolation over a limited t1/2 range and is not a significance test; the Boyd intercept test is the more reliable discriminator and is the basis of the statement above.

Because the desorption data are much less scattered than the adsorption data, the fitted parameters of the desorption branch are determined with better precision, and they are the basis of the hysteresis discussion in Section 5.2.

4.3. Thermodynamic Behavior of Calcium Carbonate Precipitates on the Adsorption of OFL

Based on the 8 h equilibrium time determined in the kinetic experiments, isothermal adsorption experiments were carried out at 5, 15, and 25 °C (Group 2). The Langmuir and Freundlich models were fitted by nonlinear regression and, as an independent mechanistic check, the Dubinin–Radushkevich (D-R) isotherm was also applied; The relevant results are presented in the analysis below. The corresponding higher-temperature dataset (Group 1: 15, 25, and 35 °C) is presented in Figure 9 and Table 6.

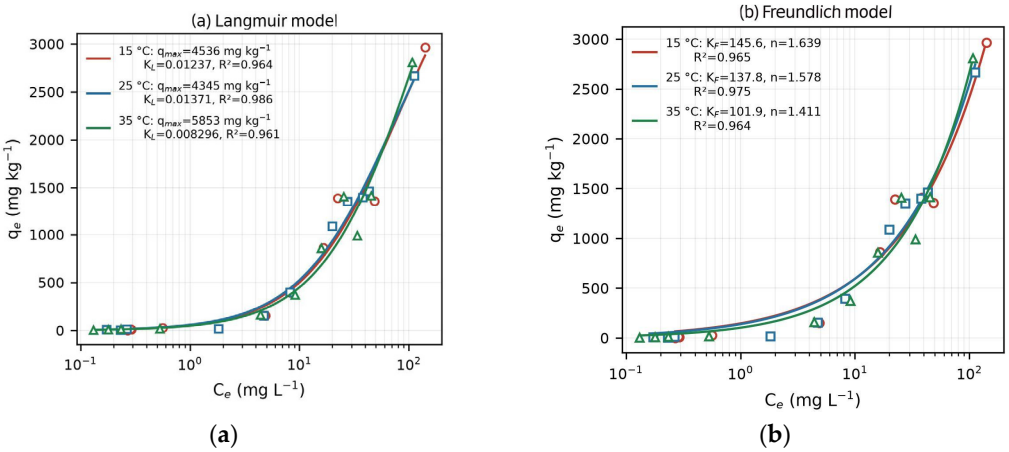


Figure 9. Adsorption isotherms of OFL on the sediments at 15, 25, and 35 °C (Group 1; 11 data points per temperature), with nonlinear fits. (**a**) Langmuir model (nonlinear fit); (**b**) Freundlich model (nonlinear fit).

As shown in Figure 10, within the experimental concentration range, the equilibrium adsorption capacity of the sediments for OFL increases with the equilibrium concentration, exhibiting a typical L-shaped isotherm. In the low-concentration region, the adsorption capacity increases rapidly, indicating the presence of high-energy adsorption sites; as the concentration increases further, these sites are progressively occupied and the curve flattens.

Both models reproduce the measured isotherms closely, but they are statistically indistinguishable over the concentration range studied. For the Group 2 dataset, the Langmuir fit returns R^2 = 0.992–1.000 and the Freundlich fit R^2 = 0.9996–1.000, and the AIC values favor the Freundlich model at 5 and 15 °C (differences of 15.1 and 9.2) while favoring Langmuir at 25 °C (difference 4.7) (Table 7). The Langmuir saturation capacities returned are 7.95 × 108, 2.25 × 109, and 2541 mg kg^{-1} at 5, 15, and 25 °C, respectively. The first two are physically meaningless: with only five data points, of which two carry almost all the information, q_{max} and K_L are strongly correlated and q_{max} is not identifiable, which is why the fit drifts towards the upper bound of the parameter while its nominal standard error remains small. The value obtained at 25 °C, where four points spanning a wider concentration range are available, is 2541 ± 98 mg kg^{-1} and is well constrained. For the Group 1 dataset, which has eleven points per temperature, the Langmuir q_{max} values are 4536 ± 686 (15 °C), 4345 ± 458 (25 °C), and 5853 ± 1490 mg kg^{-1} (35 °C), and the model preferred by AIC is Langmuir at 25 °C but Freundlich at 15 and 35 °C, the latter by less than one AIC unit (Table 6). The Freundlich exponent *n* is positive in every case (n = 0.749–1.639) and the reciprocal 1/n lies between 0.61 and 1.34, so the isotherms are favorable or close to linear. The negative *n* values (−1.336, −1.047, and −0.705 and −1.229, −1.086, and −0.803) reported in the original Tables 7 and 8 were artefacts of the linearized regression and have been removed because a negative *n* is not physically admissible for the Freundlich model.

Table 6. Langmuir, Freundlich, and Dubinin–Radushkevich parameters for the adsorption of OFL on the sediments.

T (°C)	Langmuir q_{max} (mg kg^{-1})	K_L (L mg^{-1})	$R2_L$	Freundlich K_F	n	$R2_F$	K_d (L kg^{-1})	RMSE	AIC_L	AIC_F	D-R E (kJ mol^{-1})
15	4536 ± 686	0.01237 ± 0.00346	0.964	145.6 ± 36.3	1.639 ± 0.152	0.965	23.9 ± 2.4	169.0	116.86	116.74	0.093
25	4345 ± 458	0.01371 ± 0.00256	0.986	137.8 ± 29.5	1.578 ± 0.128	0.975	27.9 ± 2.5	98.3	104.93	111.45	0.083
35	5853 ± 1490	0.008296 ± 0.00323	0.961	101.9 ± 29.7	1.411 ± 0.138	0.964	28.9 ± 2.1	167.3	116.63	115.69	0.090

Table 7. Langmuir, Freundlich, and Dubinin–Radushkevich parameters for the adsorption of OFL on the sediments (Group 2: 5, 15, and 25 °C; 4–5 data points per temperature).

T (°C)	Langmuir q_{max} (mg kg^{-1})	K_L (L mg^{-1})	$R2_L$	Freundlich K_F	n	$R2_F$	K_d (L kg^{-1})	RMSE	AIC_L	AIC_F	D-R E (kJ mol^{-1})
5	7.95×10^{8}	1.50×10^{-7}	0.992	58.2 ± 5.7	0.749 ± 0.026	1.000	119.0 ± 4.2	41.9	41.35	26.28	0.245
15	2.25×10^{9}	7.71×10^{-8}	1.000	159.5 ± 3.5	0.955 ± 0.011	1.000	173.6 ± 1.1	8.1	24.89	15.68	0.394
25	2541 ± 98	0.03655 ± 0.00214	1.000	132.0 ± 7.5	1.418 ± 0.043	1.000	59.4 ± 3.3	3.3	13.64	18.36	0.247

Table 8. Langmuir, Freundlich, and Dubinin–Radushkevich parameters for the desorption of OFL from the sediments (Group 2: 5, 15, and 25 °C), together with the linear partition coefficients.

T (°C)	Desorption Langmuir q_{max} (mg kg^{-1})	K_L (L mg^{-1})	$R2_L$	Freundlich K_F	n	$R2_F$	K_d (L kg^{-1})	RMSE	AIC_L	AIC_F	D-R E (kJ mol^{-1})
5	8.54×10^{8}	2.22×10^{-7}	0.997	126.8 ± 10.3	0.813 ± 0.030	1.000	189.3 ± 4.1	28.5	37.50	26.30	0.347
15	1.59×10^{9}	1.68×10^{-7}	0.999	231.0 ± 9.8	0.921 ± 0.021	1.000	267.2 ± 3.1	19.7	33.81	25.68	0.429
25	1.29×10^{9}	7.04×10^{-8}	0.998	68.2 ± 3.7	0.892 ± 0.018	1.000	90.8 ± 1.5	18.6	27.38	16.35	0.241

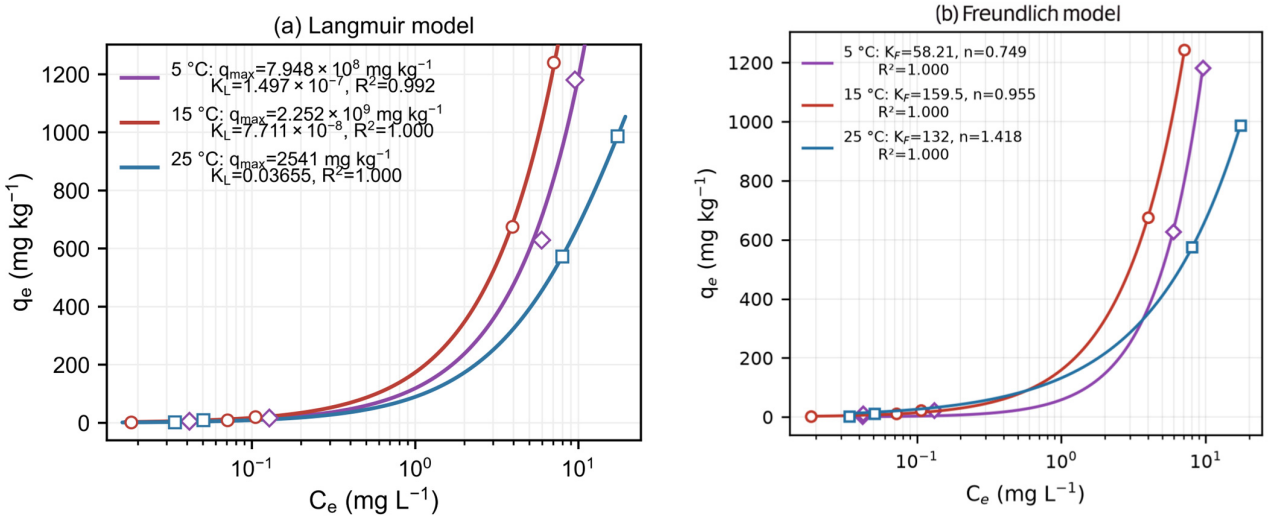


Figure 10. Adsorption isotherms of OFL on the sediments at 5, 15, and 25 °C, with nonlinear fits. (**a**) Langmuir model (nonlinear fit); (**b**) Freundlich model (nonlinear fit).

Temperature has a limited and non-monotonic effect on the adsorption capacity in the Group 2 dataset: from 5 to 15 °C, the maximum measured adsorption increases only slightly, from 1183 to 1243 mg kg^{-1}, whereas at 25 °C, it falls to 987 mg kg^{-1}. Because this sequence is not monotonic, a single van't Hoff relation cannot describe it, and no enthalpy was derived from this dataset: fitting the three points would give Delta-H = +422 ± 282 kJ mol^{-1}. The Group 1 dataset (15, 25, and 35 °C) behaves in a way that is better suited to thermodynamic analysis, and the corresponding parameters are given below.

Thermodynamic parameters were calculated from the Group 1 Langmuir constants using Equations (19) and (20), and the results are collected in Table 9. The dimensionless equilibrium constant decreases from 4955 at 25 C to 2998 at 35 C, and dG0 is close to −20 kJ mol^{-1} at all three temperatures (−20.14, −21.09, and −20.51 kJ mol^{-1} at 15, 25, and 35 °C), so adsorption is spontaneous over the whole temperature range studied. The van't Hoff regression of ln K0 on 1/T gives dH0 = −14.5 ± 13.2 kJ mol^{-1} and dS0 = 20.5 ± 44.3 J mol^{-1} K^{-1} (R^2 = 0.547), that is, a small negative enthalpy and a small positive entropy. The magnitude of dH0 is well below the 40 kJ mol^{-1} threshold usually taken to indicate chemisorption, and the enthalpy is not statistically distinguishable from zero at the 95% level, so the data support a weakly exothermic, predominantly physical interaction rather than strong chemical bonding. This is consistent with the D-R free energies of the Group 1 dataset (E = 0.083–0.093 kJ mol^{-1}, Table 6) and with the observation that the capacity changes by less than 20% between 15 and 35 °C. Because the enthalpy term is not significant, the temperature dependence of the capacity in this system is weak, and the practical consequence for the Ili River is therefore limited: the sediment retains OFL over the range of water temperatures normally encountered, and temperature mainly modulates desorption rather than changing the adsorption capacity by a large factor.

Table 9. Thermodynamic parameters for the adsorption of OFL on the calcareous sediments (Group 1).

T (°C)	T (K)	K_L (L mg^{-1})	K^0 (-)	dG^0 (kJ mol^{-1})
15	288.15	0.01237	4469	−20.14
25	298.15	0.01371	4955	−21.09
35	308.15	0.008296	2998	−20.51

Note: the uncertainties of dG0 follow from those of KL; dH0 = −14.5 ± 13.2 kJ mol^{-1} and dS0 = 20.5 ± 44.3 J mol^{-1} K^{-1} are the standard errors of the van't Hoff regression (R^2 = 0.547).

4.4. Consistency of the Fitted Capacities with the Measured Surface Area

First, the maximum adsorption measured in the Group 1 experiments was 2962.8 mg kg^{-1} (15 °C, Ce = 140.8 mg L^{-1}). Second, the mass-balance ceiling for a batch experiment at the initial concentration of the last isotherm level (259.3 mg L^{-1}) and a liquid-to-solid ratio of 25 L kg^{-1} is 6482 mg kg^{-1}, so none of the measured or fitted capacities violates mass conservation; a fitted q_{max} of 36 181 or 49 103 mg kg^{-1}, by contrast, would require an initial concentration of 1447 or 1964 mg L^{-1}, i.e., five to eight times the highest concentration used, which is a further indication that those values were not identifiable from the data (Figure 11). Third, a monolayer capacity calculated from the estimated specific surface area (3–4 m^2 g^{-1}, Section 3.1.3) with a molecular footprint of 1.0 nm^2 for a flat-oriented OFL molecule is 1800–2400 mg kg^{-1}, which brackets the measured maximum of 2962.8 mg kg^{-1} to within about 25%. The agreement between the measured capacity and the surface-area estimate, and its disagreement with the very large fitted values, supports the conclusion that the Langmuir q_{max} obtained from the 11-point Group 1 dataset (4300–5900 mg kg^{-1}) is physically reasonable, whereas the unconstrained values obtained from the 4–5-point Group 2 dataset are not.

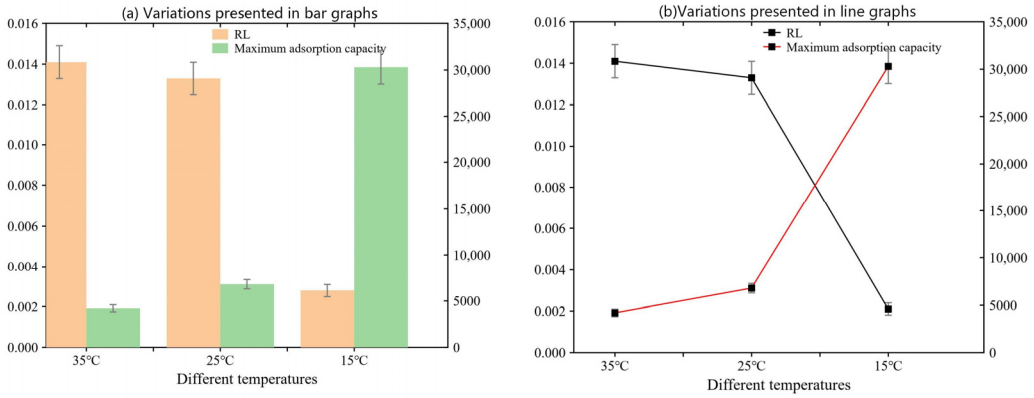


Figure 11. Variations of separation factor and maximum adsorption capacity with temperature. (**a**) Variations presented in bar graphs; (**b**) Variations presented in line graphs.

4.5. Thermodynamic Behavior of Desorption of OFL from Calcium Carbonate Precipitates

The desorption isotherms of OFL at 5, 15, and 25 °C (Group 2) are shown in Figure 12 and Table 8. The desorbed amount increases with the amount previously adsorbed. Both models fit the desorption branches closely ($R^2 \geq 0.997$), and the Freundlich model is preferred by AIC at all three temperatures (differences of 11.2, 8.1, and 11.0). As for adsorption, the Langmuir q_{max} of the desorption branches is not identifiable for the 5 and 15 C datasets (fitted values 8.54 × 108 and 1.59 × 109 mg kg^{-1}), and such values are therefore not quoted as capacities.

At 5, 15, and 25 °C, the Freundlich exponents of the desorption branches are n = 0.813, 0.921, and 0.892, so 1/n decreases from 1.23 to 1.09 and then increases marginally to 1.12; that is, the desorption isotherms become slightly more linear as the temperature rises from 5 to 15 °C and then change little. The linear partition coefficients of the desorption branches are Kd = 189.3 ± 4.1, 267.2 ± 3.1, and 90.8 ± 1.5 L kg^{-1} at 5, 15, and 25 °C (Table 8), i.e., 1.6–2.9 times the corresponding adsorption values (119.0, 173.6, and 59.4 L kg^{-1}, Table 7). The internal consistency of these numbers is supported by the fact that the desorption Kd exceeds the adsorption Kd at every temperature, which is the operational definition of hysteresis.

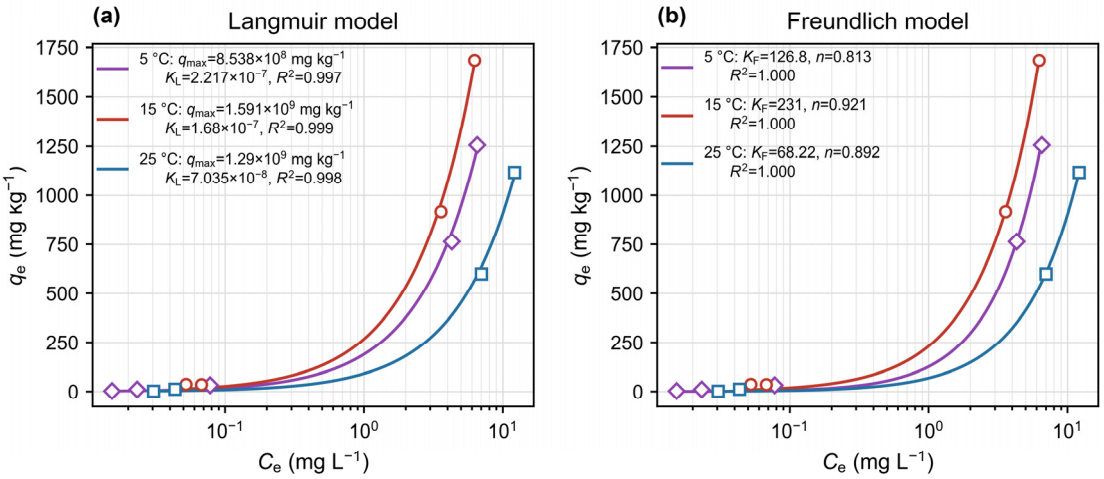


Figure 12. Desorption isotherms of OFL from the sediments at 5, 15, and 25 °C (Group 2), with nonlinear fits. (**a**) Langmuir model (nonlinear fit); (**b**) Freundlich model (nonlinear fit).

Desorption hysteresis is evident at all three temperatures: the desorption isotherms lie above the corresponding adsorption isotherms, the maximum desorbed amount exceeds the maximum adsorbed amount (ratio 106.5% at 5 °C, 135.7% at 15 °C, and 113.3% at 25 °C), and the Freundlich-based hysteresis index H = (1/nd − 1/na)/(1/nd) is −0.09, 0.04, and 0.37 at 5, 15, and 25 °C. H is small at 5 and 15 °C and clearly positive at 25 °C, so hysteresis is most pronounced at the highest temperature examined and the retention of OFL is strongest at 5 °C and weakest at 25 °C, which means that the risk of release increases with temperature. The hysteresis is consistent with the mineralogy of the sediment: interlayer retention by the smectitic component of the illite/smectite mixed layer and surface complexation on the carbonate phases both create a population of sites from which OFL is released more slowly and less completely than it is taken up.

5. Discussion

5.1. Adsorption Approaches Saturation as the Concentration Increases and Is Only Weakly Temperature-Dependent

Figure 9 shows the adsorption isotherms of qe against Ce for the Group 1 dataset. Throughout the adsorption process, the equilibrium adsorption capacity of the sediment increases with the equilibrium concentration, and because the number of accessible sites greatly exceeds the number of OFL molecules at low concentration, the uptake rises steeply at first; as the concentration increases, the sites approach saturation and qe tends to a plateau. The isotherm is therefore of the L type, which by itself indicates that the affinity of the surface for OFL decreases as coverage increases, but does not discriminate between monolayer and multilayer uptake.

Across the Group 1 temperatures (15, 25, and 35 °C), the fitted Langmuir q_{max} values are 4536 ± 686, 4345 ± 458, and 5853 ± 1490 mg kg^{-1} and the Langmuir constants are KL = 0.0124, 0.0137, and 0.00830 L mg^{-1} (Table 6). The differences between these values are comparable with their standard errors, so the temperature dependence of the capacity is weak and is not statistically resolved by this dataset; in particular, the apparent increase of q_{max} at 35 °C is not significant.

Fitting the adsorption of OFL on sediment from a specific sewage outlet of the Ili River with the Langmuir and Freundlich models allows the assumptions of those models to be examined. The isotherms at the three Group 1 temperatures, together with the nonlinear fits, are shown in Figure 9, and the parameters are listed in Table 6. The Langmuir R^2 values are 0.964, 0.986, and 0.961 and the Freundlich R^2 values are 0.965, 0.975, and 0.964, i.e., the

two models are statistically indistinguishable at 15 and 35 °C (difference in AIC $\leq$ 1) and Langmuir is preferred at 25 °C (difference 6.5). It is a general property of these two models that, over a restricted concentration range, both can fit the same data closely even when the underlying mechanism is single-valued; a good simultaneous fit therefore cannot be used as evidence that monolayer and multilayer adsorption operate together. Discriminating the two requires either an explicitly multilayer model such as BET or an independent measure of the surface area and the molecular footprint, and the D-R analysis applied here indicates a physisorption-dominated process (E = 0.083–0.247 kJ mol^{-1}, Table 6).

The Freundlich model describes adsorption on a heterogeneous surface and its exponent 1/n measures the degree of nonlinearity; it is an empirical equation and does not by itself imply multilayer coverage, so it cannot be used to demonstrate that multilayer adsorption occurs. The fitted exponents for the Group 1 dataset are *n* = 1.639, 1.578, and 1.411 at 15, 25, and 35 °C, so 1/n = 0.61, 0.63, and 0.71. Because 1/n lies between 0.5 and 1, the isotherms are favorable but only moderately so, and they become progressively more linear as the temperature increases, i.e., the surface behaves as if it were more homogeneous in its effective affinity at higher temperatures. The separation factor $R_L = 1/(1 + K_L\ C0)$ ranges from 0.27 to 0.38 over the initial concentrations used, and over the environmentally relevant range 0.1–200 mg L^{-1}, it remains below 1, confirming that the adsorption of OFL on these sediments is favorable at every concentration examined.

5.2. Desorption Becomes More Linear and More Complete at Higher Temperatures

The Langmuir and Freundlich models both fit the Group 2 isotherms closely across the three temperatures, with $R^2 \geq 0.997$, but the model preferred by AIC is Freundlich at 5 and 15 °C and Langmuir at 25 °C, and the Langmuir qmax is not identifiable for the 5 and 15 °C datasets (Section 4.3). For the Freundlich model, KF first increases and then decreases with temperature (58.2, 159.5, and 132.0 for adsorption at 5, 15, and 25 °C), which indicates a maximum in the effective affinity at 15 °C rather than a monotonic temperature effect. The exponent *n* of the adsorption branch is 0.749, 0.955, and 1.418, so the isotherm becomes progressively less curved as the temperature rises and 1/n falls from 1.34 to 0.71. The inflection in KF at 15 °C, together with the non-monotonic sequence of maximum capacities (1183, 1243, and 987 mg kg^{-1}), is the reason why the 5/15/25 °C dataset is excluded from the thermodynamic analysis in Section 4.3: a single van't Hoff relation cannot represent a maximum, and applying one would yield an enthalpy of the wrong sign and magnitude. Group 2 does, however, provide the desorption branch, and it shows that at 25 °C, the hysteresis index rises to 0.37 while the desorption Kd falls to 90.8 L kg^{-1}, so the ability of the sediment to hold OFL is weakest at the highest temperature examined. In terms of the retention mechanism, the hysteresis is best explained by interlayer capture by the smectitic component and by surface complexation on the carbonate phases, both of which create a fraction of strongly bound OFL that is released only slowly; this gives the riverbank sediment a dual sink-source character.

5.3. Acidic Conditions Significantly Enhance the Adsorption Effect of Calcium Deposits

Different pH values significantly influence the adsorption and desorption behavior of OFL in the sediments. For the Ili calcareous sediments, as the pH increases from 5 to 9, the equilibrium adsorption decreases continuously and reaches a maximum at pH 5, so an acidic environment favors adsorption, whereas the equilibrium desorption passes through a maximum at pH 7 and the overall desorption rate remains high (60–70%) (Figure 13) The interpretation rests on the speciation of OFL (pKa1 ~6.0 and pKa2 ~8.3, so the molecule is predominantly cationic below about pH 6, zwitterionic between about pH 6 and 8.3, and anionic above about pH 8.3) and on the surface charge of the sediment. Because the point

of zero charge of these samples was not measured (Section 3.1.3), the surface-charge part of the argument is stated qualitatively: carbonate and clay minerals are predominantly negatively charged at the natural pH of the study area (7.5–8.5), so the observed trend is consistent with electrostatic attraction at low pH and increasing repulsion as the anionic fraction grows. The buffering capacity of the carbonate cementation phases damps the effect of abrupt pH changes on the interfacial reaction, which may partly explain why the adsorption does not collapse at pH 9.

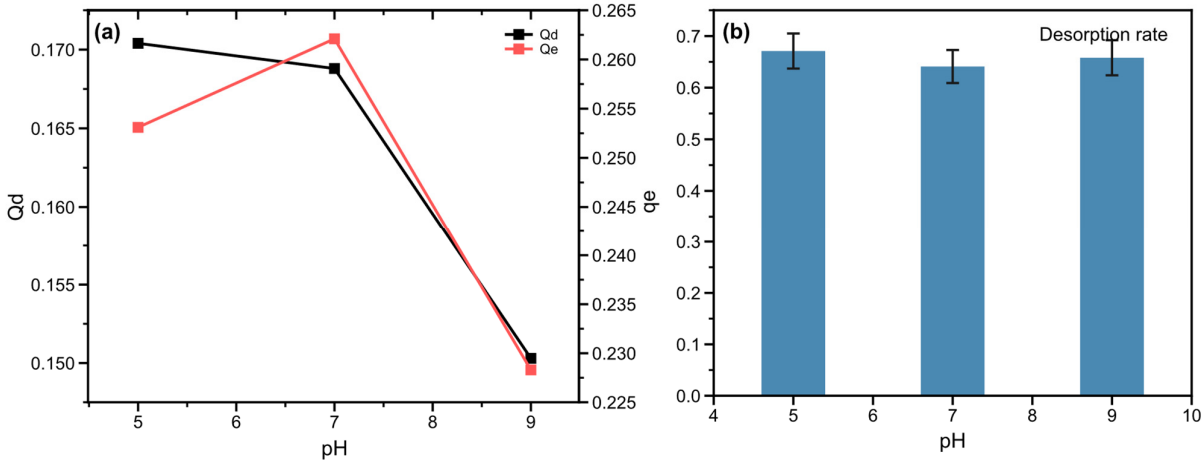


Figure 13. Effect of pH on the adsorption/desorption of OFL in sediment. (**a**) Adsorption capacity qd and equilibrium adsorption capacity q_e as a function of the initial solution pH; (**b**) desorption rate at pH 5, 7 and 9. Error bars denote the standard deviation.

5.4. Coexisting Cations Inhibit Adsorption Through Both Specific Competition and a General Ionic Strength Effect

The adsorption of OFL onto the sediments is inhibited by coexisting cations, and the extent of the inhibition depends on the valence state, ionic radius, and concentration of the cation. Two distinct effects must be separated. The first is a non-specific electrostatic (ionic strength) effect: any cation, regardless of identity, compresses the diffuse double layer of the negatively charged sediment surface and screens the electrostatic attraction between the surface and the cationic or zwitterionic form of OFL. The second is specific competition, in which a cation binds at the same surface sites as OFL by, for example, exchanging with the Ca^{2+} and Mg^{2+} of the carbonate surface or competing for the exchange sites of the smectitic interlayer. The two effects are normally superimposed, which is why an inhibition order measured across cations of different valence cannot be attributed to specific competition alone. The experimental design used here was therefore arranged so that the two contributions can be examined separately (Section 3.2.4).

Mg^{2+} and Ca^{2+} are both divalent, but the ionic radius of Mg^{2+} (0.072 nm) is smaller than that of Ca^{2+} (0.100 nm), so Mg^{2+} has the higher charge density and, at the same molar concentration, the larger hydration energy and the greater hydrated radius. In the measured series, Mg^{2+} produced the strongest inhibition of the cations tested, with an adsorption fraction of 0.036 at 0.01 mol L^{-1}, against 0.695 for Na^{+} at the same molarity and 0.185–0.452 for Ca^{2+} at 0.05–0.1 mol L^{-1} (Figure 14). The higher charge density of Mg^{2+} increases its affinity for the negatively charged sites, which is the conventional explanation for the stronger inhibition. A second effect acts in the opposite direction and deserves to be stated explicitly: because Mg^{2+} has the larger hydrated radius, its access to the narrow interlayer and mesopore sites is more restricted than that of Ca^{2+}, so at sterically constrained sites, the advantage conferred by its charge density is partly offset. The fact

that Mg^{2+} nevertheless inhibits more strongly than Ca^{2+} despite this offset indicates that the charge-density (specific competition) effect remains dominant in this sediment.

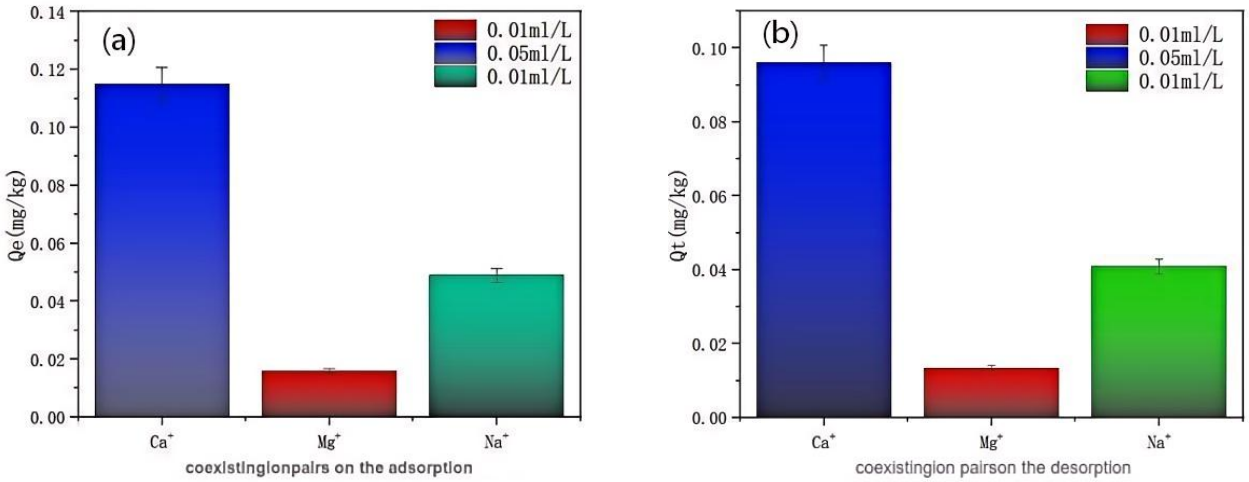


Figure 14. Effect of coexisting ion pairs on the adsorption/desorption of OFL in sediments. (**a**) On the adsorption; (**b**) On the desorption.

Ca^{2+} and Na^{+} differ in valence. Ca^{2+} is divalent and Na^{+} is monovalent, and according to the selectivity rule based on valence, the binding energy of a divalent cation to the negatively charged exchange sites of clay surfaces is appreciably higher than that of a monovalent cation, so at comparable concentrations, Ca^{2+} inhibits adsorption more strongly than Na^{+}. It should be noted, however, that at equal molarity, the ionic strength of a divalent salt is three times that of a monovalent salt, so part of the difference between Ca^{2+} and Na^{+} is electrostatic in origin rather than specific. This is precisely why Na^{+} was included in the design as an ionic strength control: the difference between Mg^{2+} and Na^{+} at matched molarity is the cleanest measure of specific competition in this dataset because the two differ in valence while the comparison is made at the same molar concentration.

At low concentrations, Na^{+} only weakly attenuates the electrostatic interaction, through compression of the diffuse double layer, and its effect on adsorption is small, giving the highest adsorption fraction of the cations tested (0.695 at 0.01 mol L^{-1}). At higher concentrations, the ionic strength effect becomes appreciable and Na^{+} would be expected to inhibit more strongly. Ca^{2+}, by contrast, produces a marked inhibition at a comparable order of concentration (0.185 at 0.05 mol L^{-1}), which is consistent with site competition operating in addition to the electrostatic effect, and its dose dependence is correspondingly steeper.

For Mg^{2+} relative to Na^{+}, the valence (charge density) effect and the radius effect act on the same side, so the difference between them is the largest of the pairwise comparisons, matching the measured order. These results have a practical implication for the high-mineralization waters of arid regions: during the low-flow season, evaporative concentration raises the concentrations of Ca^{2+} and Mg^{2+} in the water, which weakens the ability of the sediment to retain antibiotics and increases their mobility and ecological risk. It should be emphasized that the concentrations used here (0.01–0.1 mol L^{-1}) were chosen to match the ionic strength of arid-region surface waters rather than trace levels, and that these experiments cannot predict the behavior of an actual sewage effluent, which also contains dissolved organic matter, competing micropollutants, and suspended solids; the trends reported here describe the intrinsic influence of the major cations and should be extrapolated to field conditions with caution.

Overall, as the cation concentration increases, the ability of the cations to compete with OFL for adsorption sites strengthens, the adsorption of OFL decreases, and its desorption

increases. This confirms that a background electrolyte and, in particular, high-valence cations, can increase the risk of desorption and release of OFL from the sediments, in agreement with the findings of Zhang R et al. [36].

5.5. Comparison with Previous Work and Environmental Implications

The capacity measured here (fitted Langmuir q_{max} of 4.3–5.9 g kg^{-1} for the 11-point dataset, with a measured maximum of 2.96 g kg^{-1}) is of the same order as values reported for ofloxacin and related fluoroquinolones on clay- and carbonate-bearing natural solids, and is markedly lower than the capacities of engineered adsorbents such as carbon-based materials [18,22] and metal-modified frameworks [30]; this is expected because the sediment was used without modification and has a specific surface area of only 3–4 m^2 g^{-1}. In contrast to engineered systems, in which uptake is often attributed to a single dominant interaction, the behavior of this natural sediment reflects the superposition of several weak interactions: cation exchange in the smectitic interlayer, surface complexation on the carbonate phases, and, at low pH, electrostatic attraction. This is why the D-R free energy is small, the Elovich model describes the kinetics best, and the enthalpy is not significant; it is also why the system should not be described as either monolayer chemical adsorption or multilayer adsorption on the basis of isotherm fitting alone.

The environmental implication is a dual role for these riverbank sediments. Under the flow conditions that were sampled, the sediment acts as a sink: Kd is 24–29 L kg^{-1} for the Group 1 series and 59–174 L kg^{-1} for the Group 2 series, and desorption is incomplete. However, the hysteresis quantified in Section 4.4, together with the weakening of retention at 25 °C and at high pH and high ionic strength, means that the sediment can also act as a source. The hysteresis index was largest at 25 °C and the desorption rate was highest at pH 5, so the risk of secondary release is greatest during the warm, low-flow season, when water temperatures reach their annual maximum and evaporative concentration raises the ionic strength of the pore water. Because the retardation factor implied by Kd is modest (a few tens of litres per kilogram), a substantial fraction of the OFL entering the riverbank sediment can be remobilized within a single seasonal cycle. Longer-term retention, and the possibility of slow release over several seasons, should be quantified with column experiments or in situ monitoring; these are identified in the outlook below as priorities for further work. Until such data are available, the parameters reported here should be used for screening-level risk assessment, and the model parameters should not be extrapolated outside the concentration range over which they were determined (0.1–200 mg L^{-1}). From a sustainability point of view, these results identify the riverbank sediment as a seasonally switchable component of the water-quality regulation service of the Ili River: the same material that buffers antibiotic inputs during the high-flow period can become a secondary source during the warm, low-flow period, when the demand for irrigation water is at its highest. Taking this seasonality into account when designing sediment-monitoring programs and discharge permits would make the control of emerging pollutants both more targeted and resource-efficient, which is itself a sustainability objective in a water-scarce basin.

6. Conclusions and Outlook

6.1. Conclusions

(1) The adsorption of OFL onto the calcareous sediments of the riverbank discharge outlets is a two-stage process, with a fast stage that is essentially complete within the first minute of contact (70–85% of the plateau at the first sampling point) followed by a slow approach to equilibrium that is complete within about 8 h. When the classical rate laws are fitted by nonlinear regression on the original q-t scale, the Elovich model gives the best

description at 1 and 10 mg L^{-1} (R^2 = 0.829 and 0.589, lowest AIC), whereas the pseudo-first-order and pseudo-second-order models give R^2 = 0.20–0.53. The high coefficients of determination previously reported for the pseudo-second-order model (R^2 > 0.98) are an artefact of fitting its linearized form and are not reproduced on the original scale. Boyd analysis indicates that intraparticle diffusion controls the rate for the two XFD datasets, whereas film diffusion also contributes for the 237–347 series, so the rate is not limited by a single diffusion step. The equilibrium adsorption capacity increases with the initial concentration of the solution.

(2) Isotherm analysis with four to eleven data points per temperature shows that the Langmuir and Freundlich models fit the data comparably (difference in AIC $\leq$ 1 at 15 and 35 °C), so the results do not justify the statement that monolayer and multilayer adsorption coexist; discriminating between them requires an explicitly multilayer model or an independent measure of the surface area. The Dubinin–Radushkevich free energy (0.08–0.25 kJ mol^{-1}) indicates a physisorption-dominated process. The fitted Langmuir capacity of the eleven-point dataset is 4.3–5.9 mg g^{-1}, which is consistent with the monolayer capacity estimated from the specific surface area (1.8–2.4 mg g^{-1}) and the mass balance of the experiments, whereas the capacities of 36–96 mg g^{-1} reported previously were unconstrained values obtained from three-point isotherms and are not physically meaningful. The van't Hoff analysis of the 15/25/35 °C dataset gives Delta-G = −20 kJ mol^{-1}, Delta-H = −14.5 ± 13.2 kJ mol^{-1}, and Delta-S = 20.5 ± 44.3 J mol^{-1} K^{-1}, so adsorption is spontaneous and only weakly exothermic, with an enthalpy that is not statistically significant.

(3) Desorption kinetics is best described by the Elovich model (R^2 = 0.929), again in preference to the pseudo-second-order model, so the release of OFL is governed by a distribution of site energies rather than by a single chemical step. Desorption hysteresis is present at all three temperatures: the maximum desorbed amount exceeds the maximum adsorbed amount (106–136%), and the hysteresis index rises from −0.09 at 5 °C to 0.37 at 25 °C, so retention is strongest at 5 °C and weakest at 25 °C. Elevated temperatures weaken the binding of OFL to the sediment surface and increase the risk of secondary release.

(4) pH is the principal environmental control on the adsorption–desorption equilibrium of OFL. As the pH increases from 5 to 9, the equilibrium adsorption capacity of the sediment for OFL decreases continuously and is maximal at pH 5, whereas the equilibrium desorption is maximal at pH 7; the overall desorption rate remains within the range of 60–70%. This is consistent with the change in the speciation of OFL from cationic through zwitterionic to anionic as the pH increases. Because the point of zero charge of the sediment was not measured, the electrostatic part of this explanation remains qualitative; hydrogen bonding and surface complexation on the carbonate phases are expected to contribute as well, and the carbonate cementation phases buffer the system against abrupt pH change.

The mechanism is as follows: in acidic environments, OFL exists mainly as the cation and is adsorbed on the negatively charged sediment surface by electrostatic attraction, giving the strongest driving force; under neutral conditions, the zwitterionic form predominates, the driving force is weaker, and some sites bind less strongly, so desorption is more likely; under alkaline conditions, the anionic form predominates, electrostatic repulsion develops, and the capacity falls further. In addition, the carbonate cementation phases of the calcareous sediment provide a buffering capacity that damps the effect of abrupt pH changes on the interfacial reaction.

(5) The coexisting cations of the aqueous phase inhibit the adsorption of OFL by competing for adsorption sites, and the inhibition depends jointly on valence, ionic radius, and hydration. At matched molarity, Mg^{2+} inhibits more strongly than Na^+, and Ca^{2+} inhibits more strongly than Na^+, so the order Mg^{2+} > Ca^{2+} > Na^+ observed experimentally combines specific competition by the divalent cations with a general ionic strength effect;

the design adopted here, in which Na^+ serves as an ionic strength control, allows the two contributions to be distinguished. The hydrated radius of Mg^{2+} is larger than that of Ca^{2+}, which restricts its access to narrow interlayer sites and partly offsets its charge-density advantage, yet Mg^{2+} remains the strongest inhibitor, so charge density dominates in this sediment.

As the concentration of the coexisting cations increases, competition with OFL for adsorption sites intensifies, the adsorption of OFL declines, and its desorption increases; a high-ionic-strength environment therefore promotes the release of OFL from the sediments and increases its mobility. The endogenous $Ca^{2+}$and Mg^{2+} released by dissolution of the carbonate cement are expected to act in the same direction, which is consistent with the buffering and pH sensitivity observed here, but the size of this contribution could not be quantified because the ion concentrations in solution before and after adsorption were not measured; it is identified in the outlook as a priority for further work.

(6) The findings contribute directly to the sustainable management of water resources in the Ili River Basin. They provide quantitative, uncertainty-bounded indicators (Kd, the desorption ratio, and the hysteresis index) with which the buffering function of riverbank sediments can be defined, measured and monitored; they identify pH, temperature, and ionic strength as the controlling variables, so that monitoring and intervention can be focused where they are most effective; and they demonstrate that retention is reversible, which justifies treating riverbank sediments as an explicit target in the control of emerging pollutants at sewage discharge outlets. In this way, the laboratory results obtained here support the design of monitoring programs, discharge limits, and seasonal management measures for a water-scarce inland river basin.

6.2. Outlook

(1) This study primarily relied on macroscopic experimental data to infer the adsorption mechanism. In future research, microanalytical techniques such as Fourier-transform infrared spectroscopy (FTIR), X-ray photoelectron spectroscopy (XPS), and scanning electron microscopy (SEM) can be employed to directly observe changes in the functional groups, elemental valence states, and microstructure of sediment surfaces before and after adsorption, thereby enabling a more precise elucidation of the interaction mechanisms between antibiotics and sediments at the molecular level.

(2) As a typical arid inland river, the Ili River exhibits highly pronounced seasonal variations in its hydrological processes. During the flood season, driven by meltwater from ice and snow as well as precipitation inputs, the river flow increases, the water level rises, and the riverbank zones enter a flooded-reduced state. Under these conditions, the pH, ionic strength, and temperature of the water body exhibit specific combined characteristics. In contrast, during the dry season, runoff decreases sharply, and the evaporation-induced concentration effect becomes intense, exposing the riverbank sediments to an oxidizing environment, which leads to a significant increase in the ionic strength and salinity of the pore water, as well as potential substantial fluctuations in pH. The differences in hydrochemical conditions at the water–sediment interface across different hydrological cycles will inevitably result in significant alterations to the adsorption and desorption behavior of OFL, thereby influencing the role transition of the sediments between “sink” and “source” states. In the future, systematic in situ monitoring and coupled laboratory simulation studies across various hydrological cycles should be conducted to establish an adsorption–desorption response model accounting for the interactions among multiple environmental factors, thereby providing data support for the accurate assessment of antibiotic migration fluxes and ecological risks under different seasonal conditions.

(3) Several measurements that would strengthen the mechanistic interpretation were not made in this study and are recommended for the next stage: the point of zero charge, the total organic carbon content, and the cation exchange capacity of the sediments; the specific surface area by N_2 physisorption; the dissolved Ca^{2+}, Mg^{2+}, and HCO_3^- concentrations before and after adsorption in order to quantify the contribution of carbonate dissolution to ionic strength; and FTIR and XPS spectra recorded before and after adsorption in order to identify the surface complexes directly rather than inferring chemisorption from kinetic fitting. A paired freeze-dried versus field-moist experiment would also allow the effect of the sample pretreatment on the measured capacity to be quantified.

(4) The predictive framework would benefit from a formal design of experiments. Because the influencing factors interact—pH changes the speciation of OFL and, hence, its sensitivity to ionic strength, and temperature changes both the speciation equilibrium and the desorption rate—a response surface design, such as a central composite design over pH, ionic strength, and temperature, would allow the interactions to be estimated explicitly. The resulting response surface could then be compared with the predictions of a machine learning surrogate model trained on the same design, which would also provide the uncertainty estimates needed before the laboratory parameters are transferred to a catchment-scale transport model.

Author Contributions: X.W.: data curation, formal analysis, methodology, software, and writing—original draft. R.L., T.Q., X.M., P.L., B.W., and A.H.: data curation, formal analysis, resources, and writing—review and editing. Y.G.: funding acquisition, conceptualization, methodology, supervision, writing—original draft, and writing—review and editing. All authors have read and agreed to the published version of the manuscript.

Funding: This research was supported by the National College Students' Innovation and Entrepreneurship Training Program, grant number 202510755014, and the Study on Source Tracing and Regulatory Technologies of Emerging Contaminants for Key Basins in Xinjiang Uygur Autonomous Region (Urumqi, Ili Prefecture) Project No. 2024659900S1-1010001.

Institutional Review Board Statement: Not applicable.

Informed Consent Statement: Not applicable.

Data Availability Statement: The raw data supporting the conclusions are available from the corresponding author upon reasonable request.

Conflicts of Interest: The authors declare no conflicts of interest.

Abbreviations

OFL	Ofloxacin
R_L	Separation factor
R^2	Coefficient of determination
adj-R^2	Adjusted coefficient of determination
RMSE	Root-mean-square error
chi^2	Reduced chi-square
AIC	Akaike information criterion
PFO/PSO	Pseudo-first-order/pseudo-second-order
IPD	Intraparticle diffusion
q_{max}	Langmuir saturation capacity
K_d	Linear partition coefficient
D-R	Dubinin–Radushkevich
E	Mean free energy of adsorption
dG^0, dH^0, dS^0	Gibbs energy, enthalpy, and entropy of adsorption

References

1. Gola, D.; Kumar Tyagi, P.; Arya, A.; Chauhan, N.; Agarwal, M.; Singh, S.K.; Gola, S. The impact of microplastics on marine environment: A review. *Environ. Nanotechnol. Monit. Manag.* **2021**, *16*, 100552. [CrossRef]
2. Li, J.; Zhang, K.; Zhang, H. Adsorption of antibiotics on microplastics. *Environ. Pollut.* **2018**, *237*, 460–467. [CrossRef] [PubMed]
3. MacKay, A.A.; Vasudevan, D. Polyfunctional Ionogenic Compound Sorption: Challenges and New Approaches To Advance Predictive Models. *Environ. Sci. Technol.* **2012**, *46*, 9209–9223. [CrossRef] [PubMed]
4. Karbalaei, S.; Hanachi, P.; Walker, T.R.; Cole, M. Occurrence, sources, human health impacts and mitigation of microplastic pollution. *Environ. Sci. Pollut. Res.* **2018**, *25*, 36046–36063. [CrossRef] [PubMed]
5. Haider, T.P.; Völker, C.; Kramm, J.; Landfester, K.; Wurm, F.R. Plastics of the Future? The Impact of Biodegradable Polymers on the Environment and on Society. *Angew. Chem. Int. Ed.* **2019**, *58*, 50–62. [CrossRef] [PubMed]
6. Huang, W.; Deng, J.; Liang, J.; Xia, X. Comparison of lead adsorption on the aged conventional microplastics, biodegradable microplastics and environmentally-relevant tire wear particles. *Chem. Eng. J.* **2023**, *460*, 141838. [CrossRef]
7. Lambert, S.; Wagner, M. Environmental performance of bio-based and biodegradable plastics: The road ahead. *Chem. Soc. Rev.* **2017**, *46*, 6855–6871. [CrossRef] [PubMed]
8. Thompson, R.C.; Olsen, Y.; Mitchell, R.P.; Davis, A.; Rowland, S.J.; John, A.W.G.; McGonigle, D.; Russell, A.E. Lost at Sea: Where Is All the Plastic? *Science* **2004**, *304*, 838. [CrossRef] [PubMed]
9. Wang, Z.; Zhang, Y.; Kang, S.; Yang, L.; Shi, H.; Tripathee, L.; Gao, T. Research progresses of microplastic pollution in freshwater systems. *Sci. Total Environ.* **2021**, *795*, 148888. [CrossRef] [PubMed]
10. Zheng, M.; Wu, P.; Li, L.; Yu, F.; Ma, J. Adsorption/desorption behavior of ciprofloxacin on aged biodegradable plastic PLA under different exposure conditions. *J. Environ. Chem. Eng.* **2023**, *11*, 109256. [CrossRef]
11. Zhou, Y.; Ashokkumar, V.; Amobonye, A.; Bhattacharjee, G.; Sirohi, R.; Singh, V.; Flora, G.; Kumar, V.; Pillai, S.; Zhang, Z.; et al. Current research trends on cosmetic microplastic pollution and its impacts on the ecosystem: A review. *Environ. Pollut.* **2023**, *320*, 121106. [CrossRef] [PubMed]
12. Li, H.; Zhang, B.; Meng, F.; Shao, S.; Xia, Y.; Yao, Y. Adsorption, natural attenuation, and microbial community response of ofloxacin and oxolinic acid in marine sediments. *Environ. Pollut.* **2024**, *347*, 123738. [CrossRef] [PubMed]
13. Zhuang, S.; Wang, J. Interaction between antibiotics and microplastics: Recent advances and perspective. *Sci. Total Environ.* **2023**, *897*, 165414. [CrossRef] [PubMed]
14. Qin, Q.; Yang, Y.; Yang, C.; Zhang, L.; Yin, H.; Yu, F.; Ma, J. Degradation and adsorption behavior of biodegradable plastic PLA under conventional weathering conditions. *Sci. Total Environ.* **2022**, *842*, 156775. [CrossRef] [PubMed]
15. Yang, W.; Lu, Y.; Zheng, F.; Xue, X.; Li, N.; Liu, D. Adsorption behavior and mechanisms of norfloxacin onto porous resins and carbon nanotube. *Chem. Eng. J.* **2012**, *179*, 112–118. [CrossRef]
16. Khan, N.A.; Ahmed, S.; Farooqi, I.H.; Ali, I.; Vambol, V.; Changani, F.; Yousefi, M.; Vambol, S.; Khan, S.U.; Khan, A.H. Occurrence, sources and conventional treatment techniques for various antibiotics present in hospital wastewaters: A critical review. *TrAC Trends Anal. Chem.* **2020**, *129*, 115921. [CrossRef]
17. Wang, L.; Li, H.; Dang, J.; Guo, H.; Zhu, Y.; Han, W. Occurrence, distribution, and partitioning of antibiotics in surface water and sediment in a typical tributary of Yellow River, China. *Environ. Sci. Pollut. Res.* **2021**, *28*, 28207–28221. [CrossRef] [PubMed]
18. Huang, Q.L.; Wang, P.; Zhang, H.; Zhang, D.; Zhou, Y. Adsorption kinetic characteristics of ofloxacin on carbon-based adsorbents of different properties. *Environ. Chem.* **2016**, *35*, 651–657. [CrossRef]
19. Qin, X.P.; Liu, F. A review of the adsorption mechanisms of fluoroquinolone antibiotics on calcareous soils in arid regions. *Hydrogeol. Eng. Geol.* **2023**, *50*, 112–120. [CrossRef]
20. Yi, L.L.; Jiao, W.T.; Chen, W.P. Adsorption characteristics of various antibiotics in soil profiles. *Environ. Chem.* **2013**, *32*, 2267–2274. [CrossRef]
21. Fu, L.; Li, J.; Wang, G.; Luan, Y.; Dai, W. Adsorption behavior of organic pollutants on microplastics. *Ecotoxicol. Environ. Saf.* **2021**, *217*, 112207. [CrossRef] [PubMed]
22. Wang, F.; Wong, C.S.; Chen, D.; Lu, X.; Wang, F.; Zeng, E.Y. Interaction of toxic chemicals with microplastics: A critical review. *Water Res.* **2018**, *139*, 208–219. [CrossRef] [PubMed]
23. Carabineiro, S.A.C.; Thavorn-Amornsri, T.; Pereira, M.F.R.; Figueiredo, J.L. Adsorption of ciprofloxacin on surface-modified carbon materials. *Water Res.* **2011**, *45*, 4583–4591. [CrossRef] [PubMed]
24. Zhang, H.; Zhou, X.; Luo, D. Calcined Bean Dregs-Hydrocalumite Composites as Efficient Adsorbents for the Removal of Ofloxacin. *ACS Omega* **2023**, *8*, 49191–49200. [CrossRef] [PubMed]
25. Huang, M.; Zhou, T.; Wu, X.; Mao, J. Distinguishing homogeneous-heterogeneous degradation of norfloxacin in a photochemical Fenton-like system (Fe_3O_4/UV/oxalate) and the interfacial reaction mechanism. *Water Res.* **2017**, *119*, 47–56. [CrossRef] [PubMed]
26. Yang, Y.; Xue, T.; Xiang, F.; Zhang, S.; Hanamoto, S.; Sun, P.; Zhao, L. Toxicity and combined effects of antibiotics and nano ZnO on a phosphorus-removing Shewanella strain in wastewater treatment. *J. Hazard. Mater.* **2021**, *416*, 125532. [CrossRef] [PubMed]

27. Liu, G.; Zhu, Z.; Yang, Y.; Sun, Y.; Yu, F.; Ma, J. Sorption behavior and mechanism of hydrophilic organic chemicals to virgin and aged microplastics in freshwater and seawater. *Environ. Pollut.* **2019**, *246*, 26–33. [CrossRef] [PubMed]
28. Zhang, S.; Cui, L.; Zhao, Y.; Xie, H.; Song, M.; Wu, H.; Hu, Z.; Liang, S.; Zhang, J. The critical role of microplastics in the fate and transformation of sulfamethoxazole and antibiotic resistance genes within vertical subsurface-flow constructed wetlands. *J. Hazard. Mater.* **2024**, *465*, 133222. [CrossRef] [PubMed]
29. Ji, J.; Peng, L.; Gao, T.; Salama, E.-S.; Khan, A.; Liu, P.; Yun, H.; Li, X. Microplastics enhanced the toxic effects of sulfamethoxazole on aerobic granular sludge and enriched antibiotic resistance genes. *Chem. Eng. J.* **2023**, *464*, 142783. [CrossRef]
30. Chen, C.-E.; Zhang, H.; Ying, G.-G.; Zhou, L.-J.; Jones, K.C. Passive sampling: A cost-effective method for understanding antibiotic fate, behaviour and impact. *Environ. Int.* **2015**, *85*, 284–291. [CrossRef] [PubMed]
31. Mao, R.; Lang, M.; Yu, X.; Wu, R.; Yang, X.; Guo, X. Aging mechanism of microplastics with UV irradiation and its effects on the adsorption of heavy metals. *J. Hazard. Mater.* **2020**, *393*, 122515. [CrossRef] [PubMed]
32. Müller, A.; Becker, R.; Dorgerloh, U.; Simon, F.-G.; Braun, U. The effect of polymer aging on the uptake of fuel aromatics and ethers by microplastics. *Environ. Pollut.* **2018**, *240*, 639–646. [CrossRef] [PubMed]
33. Naik, R.K.; Naik, M.M.; D'Costa, P.M.; Shaikh, F. Microplastics in ballast water as an emerging source and vector for harmful chemicals, antibiotics, metals, bacterial pathogens and HAB species: A potential risk to the marine environment and human health. *Mar. Pollut. Bull.* **2019**, *149*, 110525. [CrossRef] [PubMed]
34. Mei, W.; Chen, G.; Bao, J.; Song, M.; Li, Y.; Luo, C. Interactions between microplastics and organic compounds in aquatic environments: A mini review. *Sci. Total Environ.* **2020**, *736*, 139472. [CrossRef] [PubMed]
35. Wang, J.; Guo, X. Adsorption kinetic models: Physical meanings, applications, and solving methods. *J. Hazard. Mater.* **2020**, *390*, 122156. [CrossRef] [PubMed]
36. Siriprom, W.; Sangwaranatee, N.; Herman; Chantarasunthon, K.; Teanchai, K.; Chamchoi, N. Characterization and analyzation of the poly (L-lactic acid) (PLA) films. *Mater. Today Proc.* **2018**, *5*, 14803–14806. [CrossRef]
37. Meng, L.; Yang, B.; Xue, N.D. A review on environmental behaviors and ecotoxicology of fluoroquinolone antibiotics. *Asian J. Ecotoxicol.* **2015**, *10*, 76–88.
38. Ma, H.T.; Li, J.F.; Liu, F.; Chen, L. Study of the adsorption–desorption interaction characteristics of ammonia nitrogen and typical antibiotics in soil. *J. Rock Miner. Test.* **2025**, *44*, 911–925. [CrossRef]
39. Luo, Y.; Sun, Y.; Wei, X.; He, Y.; Wang, H.; Cui, Z.; Ma, J.; Liu, X.; Shu, R.; Lin, H.; et al. Detection methods for antibiotics in wastewater: A review. *Bioprocess Biosyst. Eng.* **2024**, *47*, 1433–1451. [CrossRef] [PubMed]
40. Zhang, R.; Zhang, R.; Li, J.; Cheng, Z.; Luo, C.; Wang, Y.; Yu, K.; Zhang, G. Occurrence and distribution of antibiotics in multiple environmental media of the East River (Dongjiang) catchment, South China. *Environ. Sci. Pollut. Res.* **2017**, *24*, 9690–9701. [CrossRef] [PubMed]
41. Li, S.; Shi, W.; Liu, W.; Li, H.; Zhang, W.; Hu, J.; Ke, Y.; Sun, W.; Ni, J. A duodecennial national synthesis of antibiotics in China's major rivers and seas (2005–2016). *Sci. Total Environ.* **2018**, *615*, 906–917. [CrossRef] [PubMed]
42. Zhao, X.Y.; Chen, H.; Zhao, B.; Song, Y.M.; Lu, M.Q.; Cui, J.S.; Zhang, L.L.; Li, S.J. Spatiotemporal distribution and risk assessment of quinolone antibiotics in soils across Shijiazhuang City. *Environ. Sci.* **2023**, *44*, 2233. [CrossRef] [PubMed]
43. Conde-Cid, M.; Ferreira-Coelho, G.; Arias-Estévez, M.; Fernández-Calvinho, D.; Núñez-Delgado, A.; Álvarez-Rodríguez, E.; Fernández-Sanjurjo, M.J. Adsorption/desorption of three tetracycline antibiotics on different soils in binary competitive systems. *J. Environ. Manag.* **2020**, *262*, 110337. [CrossRef] [PubMed]
44. Chen, H.Y.; Shen, R.J.; Huang, H.B.; Zhang, F.; Shi, L.; Xie, E.P.; Li, H.L.; Shi, R.; Shen, X.M. Adsorption characteristics and predictive modeling of ciprofloxacin and tetracycline in estuarine sediments of the Yangtze River Delta. *J. Rock Miner. Test.* **2025**, *44*, 1051–1068. [CrossRef]
45. Xu, D.Y.; Xie, Z.Y.; Yu, J.; Liu, J.Y.; Xu, C.H.; Deng, Z.Y.; Qu, W.T.; Hao, Q. Adsorption mechanism of magnetic Ce-modified adsorbents for ofloxacin in water. *J. Compos. Mater.* **2022**, *39*, 2750–2763. [CrossRef]
46. Hu, Y.Y.; Shen, D.L.; Luo, S.; Zong, C.L.; Chen, J.Q.; Cheng, G.H.; Yu, Y. Simulation of adsorption influencing factors for two types of fluoroquinolone antibiotics in sediments. *Environ. Chem.* **2019**, *38*, 1570–1581. [CrossRef]
47. Jia, Z.; Jiang, Y.; Sun, Y.; Huang, K.; Wu, Y. Collaborative sorption behavior of tylosin and enrofloxacin in loess soil: Implications for veterinary antibiotic fate. *Environ. Sci. Process. Impacts* **2025**, *27*, 1914–1927. [CrossRef] [PubMed]
48. Wang, X.; Zhao, Y.; Sun, Y.; Liu, D. Highly Effective Removal of Ofloxacin from Water with Copper-Doped ZIF-8. *Molecules* **2022**, *27*, 4312. [CrossRef] [PubMed]
49. Xu, Q.; Li, H.; Li, S.; Li, Z.; Chen, S.; Liang, Y.; Li, Y.; Li, J.; Yuan, M. Impact of Microplastics on Ciprofloxacin Adsorption Dynamics and Mechanisms in Soil. *Toxics* **2025**, *13*, 294. [CrossRef] [PubMed]
50. Maghsodian, Z.; Sanati, A.M.; Mashifana, T.; Sillanpää, M.; Feng, S.; Nhat, T.; Ramavandi, B. Occurrence and Distribution of Antibiotics in the Water, Sediment, and Biota of Freshwater and Marine Environments: A Review. *Antibiotics* **2022**, *11*, 1461. [CrossRef] [PubMed]

51. Wang, P.; Zhang, D.; Zhang, H.; Li, H.; Ghosh, S.; Pan, B. Impact of concentration and species of sulfamethoxazole and ofloxacin on their adsorption kinetics on sediments. *Chemosphere* **2017**, *175*, 123–129. [CrossRef] [PubMed]
52. Camara, F.A.; Ramézani, H.; Mathieu, N.; Delpeux-Ouldriane, S.; Bhatia, S.K. Mechanistic insights into pH-dependent ofloxacin adsorption on nanoporous carbons. *Phys. Chem. Chem. Phys.* **2026**, *28*, 9358–9381. [CrossRef] [PubMed]
53. Georgin, J.; Franco, D.S.P.; Ramos, C.G.; Piccilli, D.G.A.; Lima, E.C.; Sher, F. A review of the antibiotic ofloxacin: Current status of ecotoxicology and scientific advances in its removal from aqueous systems by adsorption technology. *Chem. Eng. Res. Des.* **2023**, *193*, 99–120. [CrossRef]
54. Abd Manan, T.S.B.; Khan, T.; Sivapalan, S.; Jusoh, H.; Sapari, N.; Sarwono, A.; Ramli, R.M.; Harimurti, S.; Beddu, S.; Sadon, S.N.; et al. Application of response surface methodology for the optimization of polycyclic aromatic hydrocarbons degradation from potable water using photo-Fenton oxidation process. *Sci. Total Environ.* **2019**, *665*, 196–212. [CrossRef] [PubMed]
55. Li, W.; Ma, W.; Yang, Y.; He, H.; Chen, B. Enhanced detection of monoiodoacetic acid at ng/L level by ion chromatography with novel derivatization-free pretreatment. *J. Hazard. Mater.* **2024**, *467*, 133729. [CrossRef] [PubMed]
56. Sun, Y.; Duan, R.; Li, Y.; Lu, X.; Gao, J.; Zhu, B. Adsorption kinetics of three fluoroquinolone carboxylic acids on red clay soil in five types of aqueous solutions. *AQUA—Water Infrastruct. Ecosyst. Soc.* **2025**, *74*, 159–174. [CrossRef]
57. Zhao, Y.; Geng, J.; Wang, X.; Gu, X.; Gao, S. Tetracycline adsorption on kaolinite: pH, metal cations and humic acid effects. *Ecotoxicology* **2011**, *20*, 1141–1147. [CrossRef] [PubMed]
58. Chen, M.; Alim, N.; Zhang, Y.; Xu, N.; Cao, X. Contrasting effects of biochar nanoparticles on the retention and transport of phosphorus in acidic and alkaline soils. *Environ. Pollut.* **2018**, *239*, 562–570. [CrossRef] [PubMed]
59. Liu, D.; Wang, H.; An, S.; Bhople, P.; Davlatbekov, F. Geographic distance and soil microbial biomass carbon drive biogeographical distribution of fungal communities in Chinese Loess Plateau soils. *Sci. Total Environ.* **2019**, *660*, 1058–1069. [CrossRef] [PubMed]
60. Jiang, Y.; Zhang, Q.; Deng, X.; Nan, Z.; Liang, X.; Wen, H.; Huang, K.; Wu, Y. Single and competitive sorption of sulfadiazine and chlortetracycline on loess soil from Northwest China. *Environ. Pollut.* **2020**, *263*, 114650. [CrossRef] [PubMed]

Disclaimer/Publisher's Note: The statements, opinions and data contained in all publications are solely those of the individual author(s) and contributor(s) and not of MDPI and/or the editor(s). MDPI and/or the editor(s) disclaim responsibility for any injury to people or property resulting from any ideas, methods, instructions or products referred to in the content.